



SOURCE
DATATRANSPARENT
PROCESSOPEN
ACCESS

Caldendrin and myosin V regulate synaptic spine apparatus localization via ER stabilization in dendritic spines

Anja Konietzny^{1,2}, Jasper Grendel^{1,2}, Alan Kadek^{3,4} , Michael Bucher^{1,2}, Yuhao Han^{1,2,5}, Nathalie Hertrich^{1,2}, Dick H W Dekkers⁶, Jeroen A A Demmers⁶, Kay Grünewald^{3,5,7}, Charlotte Uetrecht^{3,4,5} & Marina Mikhaylova^{1,2,*} 

Abstract

Excitatory synapses of principal hippocampal neurons are frequently located on dendritic spines. The dynamic strengthening or weakening of individual inputs results in structural and molecular diversity of dendritic spines. Active spines with large calcium ion (Ca²⁺) transients are frequently invaded by a single protrusion from the endoplasmic reticulum (ER), which is dynamically transported into spines via the actin-based motor myosin V. An increase in synaptic strength correlates with stable anchoring of the ER, followed by the formation of an organelle referred to as the spine apparatus. Here, we show that myosin V binds the Ca²⁺ sensor caldendrin, a brain-specific homolog of the well-known myosin V interactor calmodulin. While calmodulin is an essential activator of myosin V motor function, we found that caldendrin acts as an inhibitor of processive myosin V movement. In mouse and rat hippocampal neurons, caldendrin regulates spine apparatus localization to a subset of dendritic spines through a myosin V-dependent pathway. We propose that caldendrin transforms myosin into a stationary F-actin tether that enables the localization of ER tubules and formation of the spine apparatus in dendritic spines.

Keywords caldendrin; endoplasmic reticulum; myosin; spine apparatus; synapse

Subject Categories Neuroscience; Organelles

DOI 10.15252/embj.2020106523 | Received 13 August 2020 | Revised 8 November 2021 | Accepted 19 November 2021 | Published online 22 December 2021

The EMBO Journal (2022) 41: e106523

Introduction

Adaptive neuronal circuit formation, the basis of complex brain functions such as learning and memory, critically relies on the dynamic plasticity of neuronal synapses. The majority of excitatory synapses of neuronal dendrites are located on small membranous protrusions called dendritic spines. Spines are highly dynamic, actin-rich structures that can undergo extensive morphological changes, appear, disappear, or become stabilized over long time periods (weeks and months), depending on the type of synaptic input they receive (Wiegert *et al*, 2018). Within individual spines, synaptic activity induces steep Ca²⁺ transients, which are the master regulator of highly localized, activity-dependent protein and membrane turnover mediated by dendritic secretory trafficking organelles, including the smooth endoplasmic reticulum (SER) (Yu *et al*, 2006; Holbro *et al*, 2009; Hanus *et al*, 2014; Mikhaylova *et al*, 2016; Bowen *et al*, 2017; Goo *et al*, 2017; Padamsey *et al*, 2017; Kennedy & Hanus, 2019; Perez-Alvarez *et al*, 2020). Locally confined organelle transport and anchoring at dendritic spines relies on F-actin-based myosin motors, and notably the myosin V (myoV) motor family (Wang *et al*, 2008; Kapitein *et al*, 2013; Esteves da Silva *et al*, 2015; van Bommel *et al*, 2019). Two paralogs, myoVa and Vb, are very similar in terms of their regulation and function (Wang *et al*, 2008; Hammer & Wagner, 2013). They were shown to mediate the synaptic transport of various cargoes, including recycling endosomes, endo-lysosomes, SER and mRNA (Yoshimura *et al*, 2006; Wagner *et al*, 2011; Esteves da Silva *et al*, 2015; van Bommel *et al*, 2019; Perez-Alvarez *et al*, 2020). Of note, in addition to its role as a continuously moving motor, myoV can also serve as an organelle tether (Maschi *et al*, 2018; van Bommel *et al*, 2019). In a recent study on hippocampal neurons, myoV was shown to be responsible for the insertion of SER into highly active dendritic spines, which

1 RG Optobiology, Institute of Biology, Humboldt Universität zu Berlin, Berlin, Germany

2 Guest Group Neuronal Protein Transport, Center for Molecular Neurobiology, ZMNH, University Medical Center Hamburg-Eppendorf, Hamburg, Germany

3 Leibniz Institute for Experimental Virology (HPI), Hamburg, Germany

4 European XFEL GmbH, Schenefeld, Germany

5 Centre for Structural Systems Biology, Hamburg, Germany

6 Center for Proteomics, Erasmus MC, Rotterdam, The Netherlands

7 Department of Chemistry, University of Hamburg, Hamburg, Germany

*Corresponding author. Tel: +49 30209398470; E-mail: marina.mikhaylova@hu-berlin.de

changed their plastic properties compared to SER-negative spines (Perez-Alvarez *et al*, 2020). Similarly, we have previously described the involvement of myoVa in the spine localization of a more elaborate ER-derived organelle called the spine apparatus, which is a hallmark of large, stable spines (Konietzny *et al*, 2019).

As the function of myoV has been shown to depend, among others, on Ca^{2+} concentration, we hypothesize that local Ca^{2+} -signaling in the spine might be a way to fine-tune myoV-dependent organelle localization, and to mediate nonrandom, activity-dependent targeting of dendritic spines. What are the mechanisms that transduce changes in local Ca^{2+} concentrations to myoV activity? The mammalian myoV motor protein consists of two heavy chains, each of which contains six consensus-binding sites (IQ motifs) for the ubiquitously expressed Ca^{2+} -binding protein calmodulin (CaM). The IQ motifs of myoV form the so-called lever arm, which translates the force generated by ATP hydrolysis inside the motor domain into a forward movement along the actin filament. It has been proposed that the occupancy of all six IQ motifs with CaM is required for the stabilization of the lever arm, and thereby for myoV fulfilling its function as a motor (Trybus, 2008). For that reason, CaM is often referred to as an essential light chain of the myoV holoenzyme (Heissler & Sellers, 2015). CaM contains four Ca^{2+} -binding sites called EF-hands. Ca^{2+} -binding induces a conformational switch, resulting in changed interaction with its downstream targets, including myosins (Chazin, 2011; Zhang *et al*, 2012; Shen *et al*, 2016). When myoV is purified from tissue or cultured cells in the absence of Ca^{2+} (EGTA buffer), all IQ motifs are fully occupied with CaM, and myoV is present in an auto-inhibited conformation. Motor function can subsequently be activated by cargo binding (Li *et al*, 2005; Heissler & Sellers, 2016; Cao *et al*, 2019). It has also been observed that nanomolar to low micromolar concentrations of Ca^{2+} activate the motor function of myoV *in vitro*. This is generally explained by a conformational change of CaM associated with the first IQ motif (IQ1) upon binding to Ca^{2+} , which allosterically relieves the autoinhibition state (Krementsov *et al*, 2004; Trybus *et al*, 2007; Lu *et al*, 2012; Shen *et al*, 2016). Conversely, it has been repeatedly shown that raising the Ca^{2+} concentration above micromolar levels *in vitro* leads to the dissociation of CaM, likely from the second IQ motif (IQ2), which destabilizes the lever arm and stops myoV forward motion (Krementsov *et al*, 2004; Nguyen & Higuchi, 2005; Koide *et al*, 2006; Trybus *et al*, 2007). This inhibitory effect of Ca^{2+} can be rescued by the presence of excess CaM (Homma *et al*, 2000; Trybus *et al*, 2007). Altogether, although most of what we know about myoV function has been established *in vitro*, it is clear that regulation of myoV *in vivo* will depend on many different interconnected factors.

Here, we explored the mechanisms of Ca^{2+} -dependent regulation of myoV and its implications for myoV-dependent SER transport in dendritic spines of hippocampal neurons. We discovered another brain-specific calmodulin-related Ca^{2+} -binding protein, caldendrin, as a novel Ca^{2+} -dependent interactor of myoV. Caldendrin has a bipartite structure, containing a highly basic N-terminus with a high proline content and several PxxP motifs, and a C-terminal part with four EF-hand structures similar to CaM (Seidenbecher *et al*, 1998; Laube *et al*, 2002; Mundhenk *et al*, 2019). In contrast to CaM, the first EF-hand motif preferentially binds Mg^{2+} , while the second EF-hand is cryptic, which leaves EF-hands 3 and 4 to mediate Ca^{2+} -binding (Wingard *et al*, 2005; Reddy *et al*, 2014). Caldendrin adopts

a folded conformation in which the C-terminal half masks an interface in the N-terminus for protein–protein interaction, which is rapidly released by Ca^{2+} binding (Mikhaylova *et al*, 2018). It exhibits similar Ca^{2+} -binding kinetics to CaM and requires low micromolar Ca^{2+} concentrations to become activated (Reddy *et al*, 2014). In contrast to the diffusely distributed CaM, caldendrin is specifically enriched in a subset of large dendritic spines, which already preallocates its function to a selected spine population (Laube *et al*, 2002; Dieterich *et al*, 2008). Accordingly, caldendrin is implicated in various activity-dependent pathways, among them the stabilization of F-actin in dendritic spines and inositol-3-phosphate receptor (IP_3R) signaling, which are important for synaptic plasticity (Li *et al*, 2013; Mikhaylova *et al*, 2018).

In this study, we used mass spectrometry (MS) interactor screening and native MS for recombinant purified proteins combined with protein-protein-binding assays to show a direct interaction of caldendrin with a confined region of myoV containing the IQ1 motif. Using *in vitro* reconstitution and inducible motor-cargo assays in live cells, we demonstrate that caldendrin acts as an inhibitor of myosin processivity without interfering with its F-actin association. These findings were corroborated by an analysis of SER-spine-entry-dynamics in hippocampal neurons in the presence or absence of caldendrin. Our data suggest that caldendrin transitions myoV function from processive movement to stationary anchoring. In this model, the Ca^{2+} -dependent interplay between CaM and caldendrin is a way to fine-tune myoV-dependent SER positioning, which is important for the formation of the spine apparatus in a subset of dendritic spines.

Results

Caldendrin specifically interacts with a confined 49 amino-acid region of myoV containing the IQ1 motif

Previous studies on the caldendrin protein have revealed uncommon structural features and highly specialized, cell type-specific functions (reviewed in Mundhenk *et al*, 2019). Although the C-terminus of caldendrin is the closest homolog of CaM in the brain, they display differences in topology and conformation (Mikhaylova *et al*, 2006), as well as interactor binding and regulation (Tippens & Lee, 2007; Mundhenk *et al*, 2019). In our previous work, we described the ability of caldendrin to undergo conformational change upon Ca^{2+} binding, its selective enrichment in a subset of large dendritic spines and its role in stabilizing actin filaments through interaction with cortactin (Dieterich *et al*, 2008; Reddy *et al*, 2014; Mikhaylova *et al*, 2018). These characteristics place caldendrin at an ideal position to mediate the consolidation of synaptic growth following excitatory activation.

To gain further insight into the Ca^{2+} -dependent interactome of caldendrin, here we performed a biotin-streptavidin pull-down of eukaryotically produced biotinylated GFP-caldendrin (bio-GFP-cald) or bio-GFP as a control from mouse brain lysate in the presence or absence of Ca^{2+} (Fig EV1A). Mass spectrometry (MS) analysis identified a broad network of putative brain-specific caldendrin-binding partners (Dataset EV1). The obtained list of candidates was curated with a focus on the Ca^{2+} -dependency of the interaction (Fig EV1B). We found that one class of proteins, myosins, was especially

enriched in the caldendrin pull down in the presence of Ca^{2+} . We hypothesized that, since the C-terminal domain of caldendrin is structurally very similar to calmodulin (CaM), and myosins contain known CaM-binding sites (IQ motifs), those might mediate the caldendrin-myosin interaction (Fig EV1B). We decided to focus on one specific myosin, myoV, as it was shown to be a driver of cargo-transport inside dendritic spines and as such important for spine plasticity and stability (Yoshii *et al*, 2013; Esteves da Silva *et al*, 2015; Perez-Alvarez *et al*, 2020).

To verify the MS results and to further characterize the caldendrin-myosin interaction, we employed a series of co-immunoprecipitation assays. Full-length, GFP-tagged myoVa (GFP-myVa fl) was coexpressed in HEK293T cells with full-length, tagRFP-coupled caldendrin (cald-fl-tagRFP). GFP-myVa was immunoprecipitated on GFP-trap beads from HEK293T cell lysate, which had been either supplemented with CaCl_2 or with the Ca^{2+} chelator EGTA, and the presence of caldendrin was analyzed using western blot. To elucidate whether the interaction with myoVa was mediated via the caldendrin N- (aa1–136) or C-terminus (aa137–298), two truncation constructs were tested. We found that both full-length caldendrin and the caldendrin N-terminus, but not the C-terminus, interacted with myoVa specifically in the presence of Ca^{2+} (Fig 1A). These results were surprising, as we would have expected the EF-hand containing C-terminal domain of caldendrin to mediate the interaction, due to its similarity to CaM and its ability to sense Ca^{2+} . This suggests that the Ca^{2+} -sensitivity of this interaction has to rely not only on the Ca^{2+} switch in caldendrin, but also on another Ca^{2+} sensor. Further, to narrow down the binding interface on the N-terminus, we attempted to co-immunoprecipitate myoVa with smaller N-terminal fragments of caldendrin (cald-N1 [aa1–60], cald-N2 [aa61–136], cald-N3 [aa 31–90]), but we found that none of the constructs retained the ability to bind myoV (Fig. EV1D). This hints at the involvement of a more complex binding interface that requires several amino acid residues from different regions within the N-terminus.

To show that the myoVa-caldendrin interaction was indeed direct, and not mediated by an unknown adapter protein, we performed a pull-down assay using separately purified components. Here, we used untagged caldendrin which was expressed and purified from *Escherichia coli*. As an additional control, we included a Ca^{2+} -binding mutant (mut) of caldendrin that is locked in the closed

and inactive conformation (Fig EV1C; Mikhaylova *et al*, 2018). Again, caldendrin showed a clear binding preference in the Ca^{2+} condition, whereas mut caldendrin showed little to no interaction in either condition (Fig 1B), indicating that the Ca^{2+} -dependent conformational switch is required for this binding.

Next, we went on to map the binding region of caldendrin on the myoVa protein, by performing a series of co-immunoprecipitation assays using fl cald-tagRFP and various truncation constructs of GFP-myVa (Fig 1C–E), summarized in Fig 1F. We found that caldendrin specifically interacts in a Ca^{2+} -dependent manner with a 49 amino-acid fragment (aa742–791) containing part of the motor domain and the first IQ motif of myoVa (Figs 1E and F, and EV2A). As for full-length myosin, binding of caldendrin to this 49 aa fragment is mediated by the caldendrin N-terminus, and not the C-terminus (Fig EV1E).

Binding of caldendrin and CaM to the 49 amino-acid myosin Va fragment is mutually exclusive

The results of binding interface mapping suggest that CaM and caldendrin occupy very closely associated, or possibly overlapping binding sites on myoVa. Therefore, we next asked whether binding was competitive, or whether CaM and caldendrin could bind simultaneously, as this would have implications for myoV motor function. In order to test this, we expressed GFP-myVa-IQ1 (aa742–791) in HEK293T cells, coupled it to GFP-trap beads and added an excess of exogenous, recombinant CaM to make sure that all myoVa-IQ1 were fully occupied with CaM (Fig 2A). Additionally, we expressed tagRFP-cald in a separate batch of HEK293T cells and added the lysate to GFP-myVa-IQ1-CaM-coupled beads (Fig 2A). Western blot analysis showed strong binding of caldendrin in the presence of Ca^{2+} . It also revealed that the amount of CaM still bound to the beads after this incubation step was much lower in the presence of caldendrin and Ca^{2+} , compared to the Ca^{2+} -free condition (Fig 2B and C). Of note, we observed that in EGTA-supplemented cell lysate, exogenously added CaM did not seem to associate with myoVa-IQ1 (Fig 2B). This was unexpected, since according to literature, CaM should be stably associated with myosin in the absence of Ca^{2+} (Krementsov *et al*, 2004; Trybus *et al*, 2007). However, the fact that the amount of bound CaM was reduced in the Ca^{2+} /caldendrin condition suggests that caldendrin, once it is bound to myoVa-IQ1,

Figure 1. The calcium-binding protein caldendrin interacts with a 49 amino-acid region containing the first IQ motif of myosin Va in a Ca^{2+} -dependent manner.

- A Schematic showing overall domain organization of the caldendrin protein, including an unstructured N-terminal part, and four EF-hand-binding motifs in the C-terminal part. Green boxes indicate functional EF-hands, blue indicates cryptic EF-hand. The dashed line indicates where the Nt and Ct constructs were separated. Co-immunoprecipitation experiments from extracts of HEK293T cells, coexpressing full-length GFP-myosin Va (myoVa fl) and indicated caldendrin-tagRFP (cald) constructs, show that caldendrin interacts with myoVa in a Ca^{2+} -dependent manner via its N-terminus (Nt), and not via its C-terminus (Ct). Tubulin was used as a loading control for the input. MW = molecular weight marker.
- B Pull down assay indicates that recombinant purified GFP-myVa and untagged caldendrin (cald wt) directly bind to each other in a Ca^{2+} -dependent manner. Note that there is no binding observed for a Ca^{2+} -binding mutant of caldendrin (cald mut/Left panel). Right panel: neither wt nor mut caldendrin bind to GFP-coupled beads.
- C–E Mapping of the binding region between myoVa and caldendrin using co-immunoprecipitation of cald-tagRFP and GFP-myVa fragments expressed in HEK293T cells. Arrows in (D) indicate the size of the respective myosin fragment.
- F Summary of the results from (C–E). Caldendrin binds specifically to a fragment containing IQ-motif 1 (amino acids 742–791), but not to any other region of myoVa, in a Ca^{2+} -dependent manner.

Source data are available online for this figure.

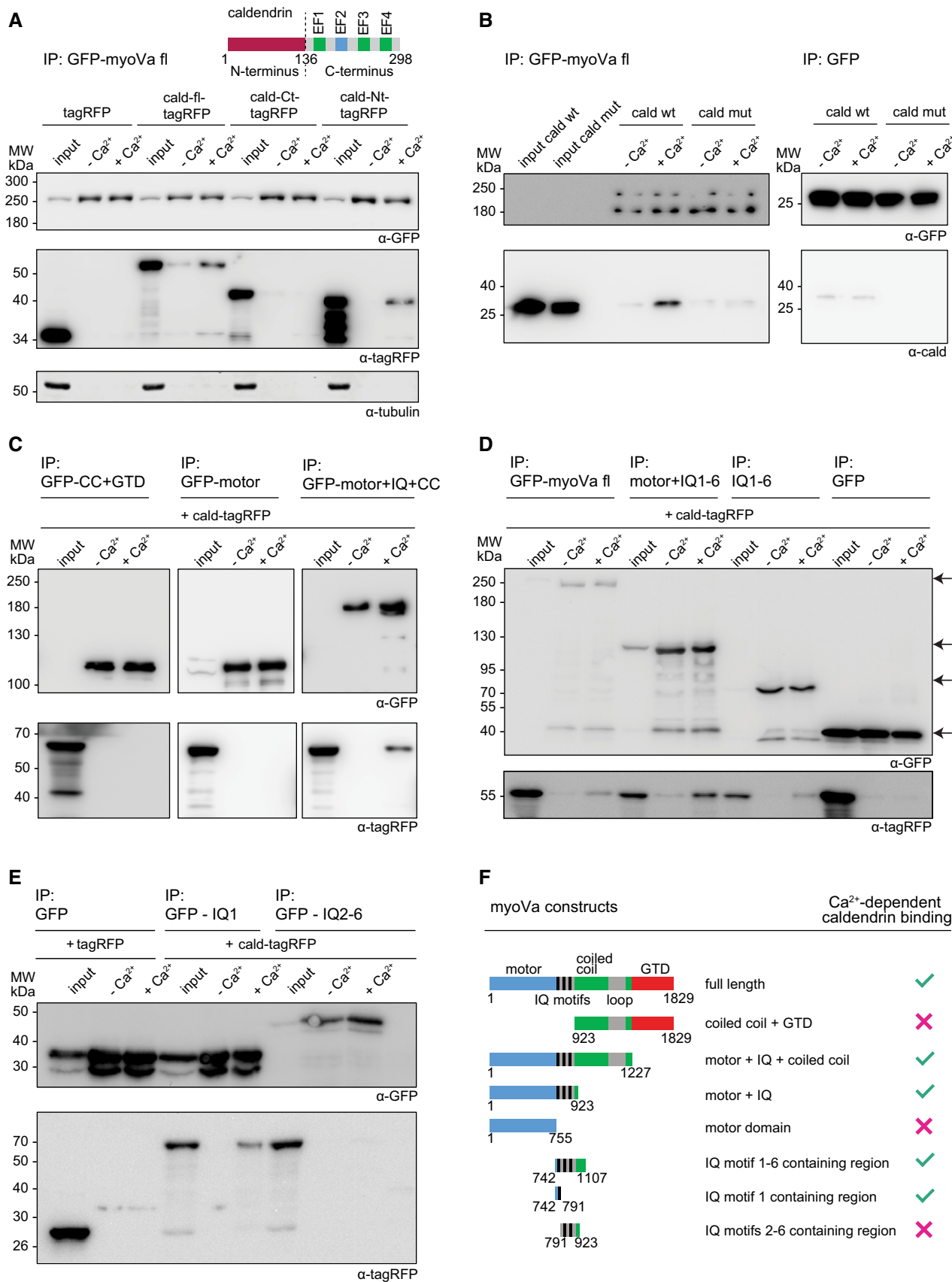


Figure 1.

prevents CaM from re-binding, or that it might even displace CaM from its binding site.

To get further insights on the complex composition in the presence of Ca^{2+} , we decided to employ a MS assay, which makes it possible to study stoichiometries of protein complexes in their native conformation. We chose to use the 49 amino-acid fragment of myoVa, which was chemically synthesized (Fig EV2A), together with CaM and caldendrin purified from *E. coli* (Fig EV2B). Since native MS interaction studies need to be carried out from a volatile aqueous solution, typically ammonium acetate, we first performed circular dichroism (CD) spectroscopy on the synthesized myosin peptide in both water and 150 mM ammonium acetate to estimate folding and potential solvent effects on its secondary structure.

Based on a published crystal structure of a myoVa fragment (aa 1–792) containing the motor domain and the first IQ motif (Coureux et al, 2004), we expected to see a high alpha-helical content, as well as some beta-sheet and loop structures (Fig EV2A). CD spectroscopy revealed distinct secondary structure elements of the myosin peptide both in water and ammonium acetate buffer, with the shape of the spectrum clearly indicating an alpha-helical fold in both solvents (Fig 2D and E). While roughly a third of the peptide sequence seems to be disordered, the rest shows the expected structural motifs (Fig 2E). Of note, due to high absorbance of the ammonium acetate below ~ 200 nm, the measured spectral range of the myosin peptide was limited to 200–260 nm (Figs 2D and EV2C).

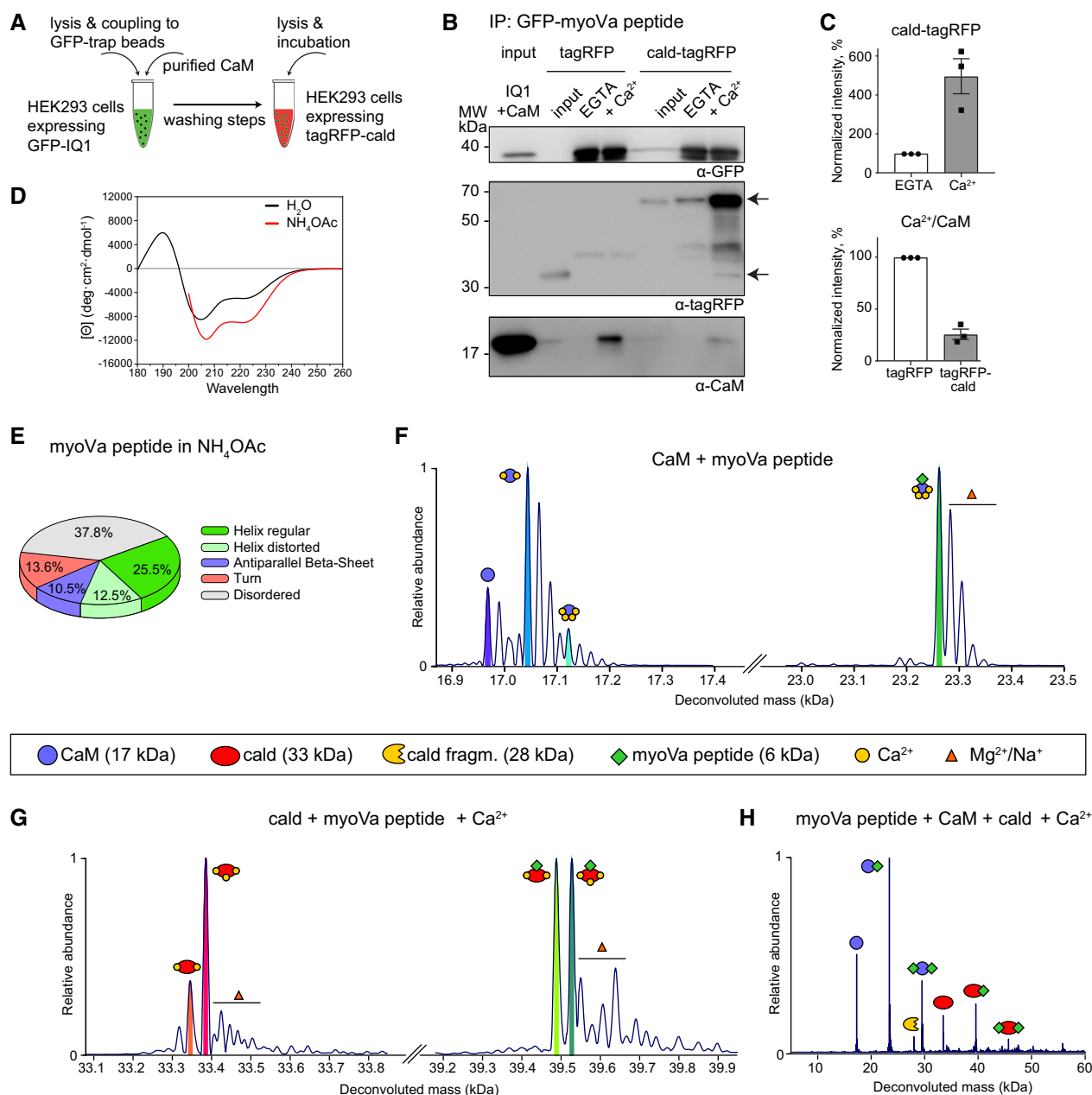


Figure 2.

Figure 2. Binding of caldendrin and calmodulin to a 49 amino-acid fragment of the myosin Va protein including the first IQ motif is mutually exclusive.

- A Schematic of caldendrin and calmodulin competition assay. A construct containing the GFP-tagged caldendrin binding peptide (aa 742–791) of myoVa (GFP-myoVa IQ1) was purified via GFP-trap beads from HEK293T cell lysate enriched with bacterially produced calmodulin (CaM). The CaM-associated construct (Input) was then incubated with lysate from HEK293T cells expressing either cald-tagRFP or tagRFP only.
- B Western blot analysis of competition co-immunoprecipitation experiment in HEK293T cells. In the presence of Ca^{2+} , caldendrin binds strongly to the IQ1 fragment (upper arrow), while tagRFP by itself does not bind (lower arrow). Detection using a calmodulin antibody indicated that Ca^{2+} -dependent binding of caldendrin reduced the amount of CaM bound to the IQ1 motif relative to the control (tagRFP only). MW, molecular weight marker.
- C Quantification of the normalized relative intensity of cald-tagRFP (left) and CaM bands (right) in western blot analysis of three independent experiments as shown in (B). Shown is mean \pm SEM. Upper: Ca^{2+} greatly increases cald-tagRFP binding to GFP-myoVa-IQ1. Lower: When Ca^{2+} is available, the simultaneous presence of cald-tagRFP leads to a reduced binding of CaM compared to the control (tagRFP).
- D CD spectroscopy reveals distinct secondary structure elements of the myoVa IQ1-containing peptide in water and ammonium acetate solution. Far-UV CD spectra of the myosin peptide acquired either in ultrapure water (black) or in ammonium acetate buffer (red; 0.5 nm step size, 3 s/point, 25 μs sample period, three repeats each, $T = 20.0 \pm 0.3^\circ\text{C}$).
- E Pie chart indicating structure elements of the myoVa IQ1-containing peptide in ammonium acetate solution calculated from spectra shown in (D).
- F Native MS analysis of ion saturation for CaM. Ca^{2+} carried along from purification is detected on CaM in native MS. Without further supplementation with ions, intact CaM shows primarily its high affinity calcium binding sites occupied (left), while in the same analysis myoVa peptide selectively and preferentially binds only to the fully Ca^{2+} -saturated CaM species (right). Additional unassigned peaks represent unspecific adducts of Na^+ and Mg^{2+} ions.
- G Native MS analysis of ion saturation for caldendrin. Supplemented by an excess of 200 μM Ca^{2+} and 100 μM Mg^{2+} , caldendrin displays myoVa peptide binding to both fully Ca^{2+} -saturated and two Ca^{2+} -bound species (right), which are also both detectable for the intact caldendrin protein in the same analysis (left).
- H No ternary complex is observed when CaM and caldendrin are mixed together with excess myoVa peptide in native MS. The individual proteins bind individually to myoVa peptide indicating competition for the same or closely located epitope. Fraction of caldendrin degrades into a 28 kDa fragment, which has lost its affinity towards myoVa peptide almost completely.

Source data are available online for this figure.

For the native MS setup, all proteins were buffer exchanged either into calcium-free ammonium acetate alone or with the addition of 200 μM CaCl_2 and 100 μM MgCl_2 . To investigate myosin peptide-binding, we compared the combination of CaM with equimolar myoVa peptide, caldendrin with equimolar myoVa peptide, and CaM plus caldendrin with 2 \times excess of myoVa peptide.

When only looking at CaM in Ca^{2+} -free solution, we saw that throughout the buffer exchange process about 75% of the purified CaM still retained two Ca^{2+} ions bound from its Ca^{2+} -containing purification buffer, 10% had four Ca^{2+} bound, and only 15% was completely free of Ca^{2+} (Fig 2F). This clear preference of even-numbered occupation states fits nicely with the presence of two high affinity and two low affinity Ca^{2+} -binding modules in CaM as described (Faas *et al*, 2011). Interestingly, the binding to the myoVa peptide was clearly Ca^{2+} -dependent as only CaM fully saturated with four Ca^{2+} ions was detected in complex with the peptide (Fig 2F). Of note, additional, unassigned peaks in the spectra correspond to unspecific sodium- or magnesium ion adducts to the protein, which is a well-known phenomenon in electrospray ionization MS (lavarone *et al*, 2004; Flick *et al*, 2012).

In the case of caldendrin, we were able to observe it in complex with the myosin peptide both in a 2 \times Ca^{2+} and 3 \times Ca^{2+} -bound state but not with the small remaining population of Ca^{2+} -free caldendrin (Fig 2G). Further, it became apparent from the spectra that part of the intact caldendrin protein (33 kDa) had degraded during purification and buffer exchange, resulting in the formation of a 28 kDa degradation product (Fig 2H). While the exact sequence of this caldendrin fragment could not be determined, it practically lost its affinity for the myosin peptide (Fig 2H). Finally, and most importantly, when all components (CaM, caldendrin, and myoVa-IQ1 peptide) were combined in the presence of Ca^{2+} and Mg^{2+} , we observed both CaM-myoVa-peptide and caldendrin-myoVa-peptide complexes (Fig 2H) but did not detect any ternary complex containing all of the proteins together. This again corroborates our previous observation indicating that the two Ca^{2+} -binding proteins compete with each other.

Caldendrin inhibits myosin V processivity *in vitro*

As Ca^{2+} /CaM bound to IQ1 is known to play a role in myoVa activation (Trybus *et al*, 2007; Lu *et al*, 2012; Shen *et al*, 2016), we asked how caldendrin binding to myoVa might affect motor function. To investigate this, we performed a reconstituted *in vitro* gliding assay. Full-length GFP-tagged myoVa was purified from HEK293 cells via a Twin-StrepTag (Fig 3A) and attached to a glass surface in a flow chamber. Alexa-568-labeled actin filaments were polymerized *in vitro* and introduced into the flow channel, where they could be observed to be “gliding” over the surface of myoVa motors (Fig 3B). Untagged CaM and caldendrin were both purified from *E. coli* (Figs EV1C and EV2B). Of note, a fraction of CaM was already associated with Ca^{2+} from the purification process as seen in the native MS (Fig 2F). In order to mimic the conditions inside an activated dendritic spine, where myoV and caldendrin would primarily interact, we based our assay conditions on work from Faas *et al* (2011) and Raghuram *et al* (2012): the cellular concentration of CaM and caldendrin were broadly estimated to be around 100 and 10 μM , respectively. Further, on the basis of up to 50 μM intracellular Ca^{2+} -levels during a calcium-spike inside a dendritic spine (Faas *et al*, 2011), Raghuram *et al* (2012) calculated the maximum concentration of Ca^{2+} -saturated protein to be around 8 μM for caldendrin, and 12 μM for CaM. To keep within this estimated 1.5–10-fold excess of CaM over caldendrin, we decided to use 30 μM CaM and 5 μM caldendrin in the F-actin gliding assay. To analyze the effect of caldendrin on the ability of myoVa to move F-actin, we took time-lapse image series of the gliding filaments and compared myoVa activity at 60 μM Ca^{2+} in the presence of CaM before and after supplementation with caldendrin. The analyzed assay parameters were the percentage of “mobile” vs. “immobile” filaments in a given field of view (Fig 3C and D), and the velocity at which the myoVa motors were propelling the mobile actin filaments (Fig 3E and F). We found that the presence of caldendrin significantly increased the fraction of immobile filaments (from an average of 19.6% to an average of 52.8%; Fig 3D). At the same time, caldendrin strongly decreased

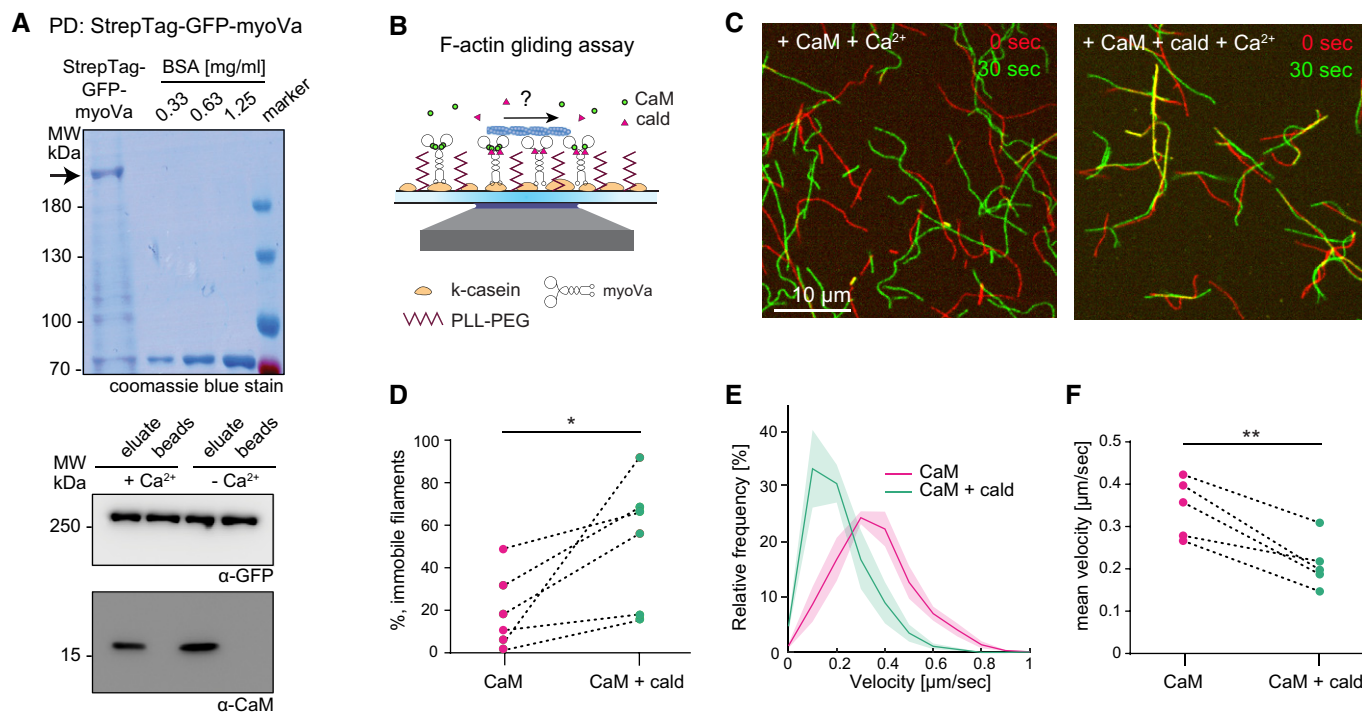


Figure 3. Caldendrin inhibits myosin Va processivity in *in vitro* F-actin gliding assay.

- A Upper: Coomassie blue-stained SDS-PAGE showing purified full-length myoVa (arrow) from HEK293T cells using a StrepTag-GFP-tag. Lower: Western blot of StrepTag-GFP-myoVa shows that myosin is associated with HEK293T-cell endogenous calmodulin (CaM) upon purification.
- B Schematic representation of *in vitro* F-actin gliding assay. CaM, calmodulin, cald, caldendrin; PLL-PEG, Poly-L-lysine-polyethylene-glycol.
- C Visualization of F-actin gliding caused by myoVa activity. The first (red) and last (green) frame of a 30 s time-lapse image stack were color-coded and overlaid to visualize movement. Yellow = actin filament did not move during 30 s of imaging. In the presence of only CaM (left), the majority of actin filaments are gliding. In the presence of both CaM and cald (right), a large number of filaments are immobile. Scale bar = 10 μ m. Also see Movie EV1.
- D Quantification of immobile filaments as shown in (C). In the presence of cald, the fraction of immobile actin filaments is significantly increased compared to CaM only (* P = 0.031, n = 6 experiments, Wilcoxon matched-pairs signed rank test). In each experiment, between 189 and 491 individual filaments were observed. Individual actin filament numbers per experiment: 275, 309, 189, 362, 390, 491).
- E Relative frequency distribution of recorded gliding velocities. In the presence of cald, the velocity distribution is shifted toward slower velocities compared to CaM only (mean \pm SEM, n = 5 experiments, eight filaments for each experiment and condition).
- F Quantification of F-actin gliding velocity. In the presence of cald, the velocity of F-actin gliding is significantly reduced compared to CaM only (mean \pm SEM, ** P = 0.0052, paired t -test, n = 5 experiments).

Source data are available online for this figure.

the average mobile filament velocity (from 344 nm/sec to 211 nm/sec; Fig 3E and F; Movie EV1). From this, we concluded that caldendrin generally inhibits myoVa activity *in vitro*.

Caldendrin does not affect the ability of myosin V to bind actin filaments

There are several ways in which caldendrin could inhibit myosin processivity. A simple explanation could be a conformational change which weakens the affinity of myoV for F-actin. However, this question could not be unambiguously answered by the gliding assay, as actin filaments can passively settle on the surface of the flow chamber without binding to myoV. Therefore, we investigated this possibility by first performing an F-actin cosedimentation assay using *in vitro* polymerized F-actin, GFP-myoVa purified from HEK293T cells (Fig 3A), and caldendrin purified from *E. coli* (Fig EV2B). When F-actin is pelleted via ultracentrifugation, F-actin-binding proteins cosediment with F-actin, while soluble proteins

(including monomeric G-actin) stay in the supernatant (Fig 4A and B). First, we made sure that the pelleting of F-actin was unaffected by the presence or absence of 50 μ M Ca²⁺ (Fig 4A). We used the non-actin-binding protein bovine serum albumin (BSA) as a control for washing, reaction tube stickiness, and “passive” pelleting with the F-actin mesh, and found the amount to be negligible (Fig 4A). While GFP-myoVa was not found in the pellet in the absence of F-actin, it cosedimented with F-actin regardless of the presence or absence of equimolar caldendrin in 50 μ M Ca²⁺ (Fig 4B). We concluded from this that the presence of Ca²⁺/caldendrin does not prevent myoVa from binding to F-actin *in vitro*.

To gain further insight into this question under physiological conditions, that is, inside a living cell, we decided to employ a previously published inducible cargo-motor-assay in COS7 cells to investigate myosin functionality *in vivo* (Kapitein et al, 2013). In this assay, peroxisomes, which are small and mostly immobile organelles, are coupled to a constitutively active kinesin-2 motor protein via a peroxisome-targeting sequence. This leads to

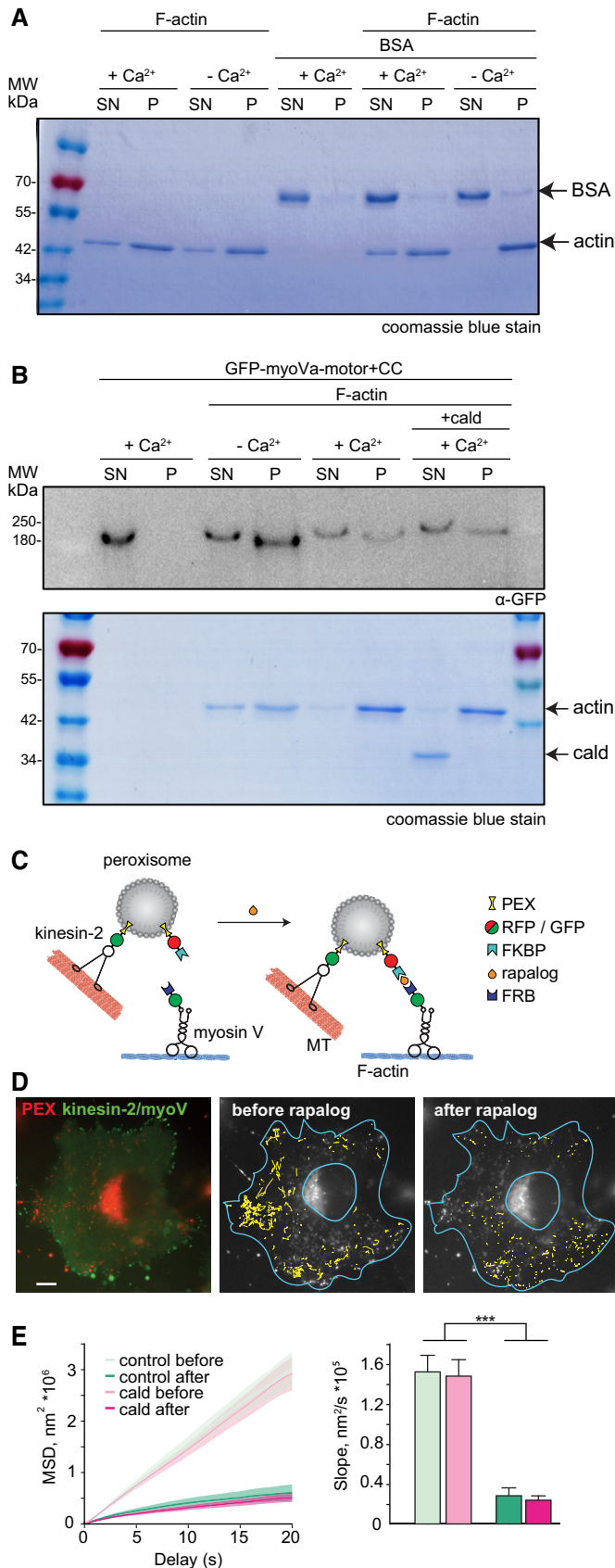


Figure 4. The presence of caldendrin does not impair the ability of myosin V to bind actin filaments *in vitro* and in live COS7 cells.

A Coomassie blue-stained SDS-PAGE showing results of F-actin cosedimentation assay. *In vitro* polymerized actin filaments sediment irrespectively of the presence and absence of calcium ions. BSA was used as a control to estimate the amount of “passively” cosedimented non-actin-binding protein and/or residual non-actin-binding protein in the pellet. There was no difference between the amount of BSA in the pellet with or without F-actin.

B Cosedimentation assay of GFP-tagged myosin fragment lacking the globular tail domain (GFP-myosin Va-motor + CC) with F-actin shows that the presence of Ca²⁺-caldendrin does not prevent myoV from binding to actin filaments. GFP-myosin Va-motor+CC, as visualized by an anti-GFP antibody via western blot, cosediments with F-actin (coomassie blue-stained SDS-PAGE), both in presence and absence of Ca²⁺, regardless of the presence of caldendrin.

C Schematic representation of the inducible transport assay in COS7 cells. Three plasmids are coexpressed in COS7 cells: a constitutively active kinesin-2 motor (KIF17) fused to a GFP-tagged peroxisome targeting sequence (KIF17-GFP-PEX13), an RFP-tagged PEX13 fused to an FKBP protein (PEX-RFP-FKBP), and a constitutively active myosin Vb motor fused to an FRB protein (myoV-GFP-FRB). Addition of the small molecule rapalog leads to dimerization of the FKBP and FRB, thus recruiting myoV to the peroxisome. Additionally, the cells were transfected with untagged caldendrin (or an empty control vector) to assess the effect of caldendrin binding to myoV on its activity in living cells.

D Left: Representative image of COS7 cell expressing the inducible dimerization system described in C. Red: Peroxisomes (PEX-RFP-FKBP), Green: KIF17-GFP-PEX13 and myoV-GFP-FRB. Scale bar = 10 μm. Middle and right: Individual tracks of kinesin-driven peroxisome movements reconstructed over 20 s (yellow) before (middle) and after (right) addition of rapalog indicate that the recruitment of myoV slows down the motility of peroxisomes. Blue outlines represent manually drawn cellular border and nucleus (excluded from analysis). Also see Movie EV2.

E Analysis of the mean squared displacement (MSD) of peroxisomes over time (left) suggests a linear increase for all conditions. Slope analysis for MSD curves for individual cells (right) indicates that addition of rapalog induces efficient stalling (2-way ANOVA, ****P* < 0.0001 as compared before and after rapalog). However, no difference between control and caldendrin (cald) transfected cells could be observed (2-way ANOVA, Mean ± SEM; *n* control = 14 cells, *n* cald = 23 cells; 3 experiments).

Source data are available online for this figure.

continuous movement of peroxisomes along microtubules all throughout the cell, and especially the cell periphery (Kapitein *et al*, 2013). Additional recruitment of myoV to the same cargo, via a rapalog dimerization module, is sufficient to stop or greatly reduce their motility due to myosin anchoring the peroxisome to F-actin (Fig 4C; Kapitein *et al*, 2013). This provides a direct readout of myoV motor activity inside the cell. We reasoned that if caldendrin decreases myoV affinity for F-actin, myoV should stall kinesin-driven peroxisomes less effectively in the presence of caldendrin. First, since caldendrin binding to myoV requires the presence of Ca²⁺, we looked into COS7 endogenous Ca²⁺ dynamics by expressing the fluorescent Ca²⁺ sensor GCaMP7s (Dana *et al*, 2019). During 5 min live imaging periods, we observed that COS7 cells spontaneously produce large intracellular Ca²⁺ transients, making it plausible that in most cells that we looked at, caldendrin would have had a chance to bind to Ca²⁺, and thereby interact with myoV (Fig EV3A, Movie EV2).

Second, for the inducible motor-cargo assay, we coexpressed three separate constructs: (i) a constitutively active, peroxisome-targeted (PEX) kinesin-fragment, (ii) PEX-FKBP (FK506 binding protein), and

(iii) a myoV motor fused to an FRB (FKBP-rapamycin-binding) domain (Fig 4C). Addition of rapalog induces the heterodimerization of FKBP with FRB, and thereby allows for a time-controlled recruitment of the myoV motor to the kinesin-coupled peroxisome. Of note, for this assay we used a myoVb construct (as published in Kapitein *et al*, 2013), which, just like myoVa, showed Ca²⁺-dependent interaction with caldendrin (Figs EV1B and EV3B, Dataset EV1). Since COS7 cells do not endogenously express caldendrin, we additionally transfected them with an untagged caldendrin construct and confirmed coexpression with the inducible motor system in fixed COS7 cells (Fig EV3C). The inducible dimerization assay showed the expected inhibition of kinesin-driven peroxisome motility by myoVb recruitment in the control condition (Fig 4D and E, Movie EV3). The efficiency of myosin-induced anchoring of peroxisomes, as assessed by the mean-squared displacement (MSD) of peroxisomes before and after rapalog addition, was not affected by the simultaneous expression of caldendrin (Fig 4E). Together with the F-actin cosedimentation data, this led us to conclude that caldendrin binding to myoV is unlikely to inhibit association of myoV with F-actin.

Overexpression of caldendrin in hippocampal neurons leads to an increase of SER localized inside dendritic spines

Any inhibitory effect of caldendrin on myoV would be especially relevant where caldendrin is present in high concentrations, that is, in a subset of dendritic spines (Laube *et al*, 2002; Smalla *et al*, 2003). At the same time, a process that relies on myoV in hippocampal neurons is the localization of SER, and of the ER-based spine apparatus organelle, to selected spines (Konietzny *et al*, 2019; Perez-Alvarez *et al*, 2020). Spinous targeting of SER can be observed during periods of high synaptic activity, that is, when Ca²⁺ concentration in an individual synapse is temporarily increased (Perez-Alvarez *et al*, 2020), which also favors activation of caldendrin (Mikhaylova *et al*, 2018). Therefore, we hypothesized that caldendrin might be involved in the regulation of SER targeting to spines by tuning myoVa activity.

To investigate this, we over-expressed GFP-tagged caldendrin in dissociated rat hippocampal neurons together with a fluorescent ER-marker (ER-tDimer2) for 18–24 h to observe SER-spine-entry dynamics in the presence of excess caldendrin. Of note, since it was not possible to additionally include a synaptic marker in this setup, here we could not definitively distinguish between spines and filopodia, which is why we refer to both collectively as “protrusions.” We later confirmed by immunostaining that caldendrin overexpression over this time interval did not alter the filopodia-to-spine ratio of dendritic protrusions (Fig EV4C).

Using live imaging, SER dynamics were recorded over a period of 10 min with 0.5 fps (Fig 5A). The frame-by-frame presence (yes/no) of SER inside a given protrusion was quantified and protrusions that contained SER during the entire imaging period were scored as having a “stable” SER insertion, others were counted as “transient” or “absent” (Fig EV4A). We found that under caldendrin overexpression, the distribution of “stable,” “transient,” and “absent” ER inside protrusions had significantly changed, with an increase in “stable” protrusions from 9 to 17% (Figs 5B and EV4A, Movie EV4). In those protrusions that experienced transient ER visits, the number of ER entries per imaging period was not affected by caldendrin overexpression, with roughly 20% of protrusions experiencing more than one ER entry (Fig EV4B).

In order to distinguish between spine-localized and filopodia-localized SER, we used immunostaining on fixed cells to visualize ER together with the post-synaptic marker homer1 (Fig 5C). Caldendrin overexpression caused an increase in both spine and filopodia density (Fig 5D and E). Consistent with the live imaging results, overexpression also significantly increased the percentage of homer1-positive spines that contained SER (19.9–24.5%, Fig 5F).

A recent study reported that about 90% of spines that contain stably inserted ER over a time period of 5 h or longer are also positive for the spine apparatus marker protein synaptopodin (Perez-Alvarez *et al*, 2020). Additionally, we have previously shown that enrichment of synaptopodin, and spine apparatus formation, depend on the activity of myoVa (Konietzny *et al*, 2019). We therefore hypothesized that overexpression of caldendrin

Figure 5. Overexpression of caldendrin leads to an increase of stable SER and the spine apparatus in dendritic spines of rat primary hippocampal neurons.

- A Example confocal images from 10 min time-lapse imaging of control (GFP) or caldendrin (cald-GFP) transfected rat primary hippocampal neurons (DIV17) expressing an ER-marker (ER-tDimer). Yellow arrows show dendritic protrusions with a stably inserted ER (> 10 min). Blue arrows indicate protrusions with a transient ER entry. Scale bar = 5 μm. Also see Movie EV4.
- B Quantification of dynamic SER presence in protrusions of control (GFP) or caldendrin (cald-GFP) transfected neurons. In protrusions of cald-GFP neurons, the percentage of stably localized ER (> 10 min) is increased, while transient SER visits are decreased compared to the control (mean ± SEM, 2-way ANOVA, **P* = 0.0386 for interaction, *n* GFP = 9, *n* cald-GFP = 10; 2 experiments).
- C Representative confocal images of control (GFP) or caldendrin (cald-GFP) transfected rat primary hippocampal neurons expressing an ER-marker (ER-tDimer). To preload overexpressed caldendrin with Ca²⁺, neurons were stimulated with 50 μM bicuculline for 5 min 8 h prior to fixation and stained with a homer1-antibody to visualize synapse-containing spines. Arrows indicate spines that contain ER. Scale bar = 5 μm.
- D–F Quantification of protrusion- and spine density and the number of SER-positive spines as shown in (C) (mean ± SEM, *n* GFP ctrl = 24 cells, *n* Cald-GFP = 25 cells; 3 experiments). (D) The density of dendritic protrusions (spines and filopodia) is increased in cald-GFP overexpressing neurons compared to the control (**P* = 0.0119, unpaired *t*-test). (E) The density of homer1-positive dendritic spines is increased in cald-GFP overexpressing neurons compared to the control (***P* = 0.0049, unpaired *t*-test). (F) The percentage of ER-containing dendritic spines is increased in cald-GFP overexpressing neurons compared to the control (**P* = 0.0179, unpaired *t*-test).
- G Representative confocal images of control (GFP) or caldendrin (cald-GFP) transfected rat primary hippocampal neurons pretreated with bicuculline as in (C) and stained against homer1 and the spine apparatus-marker synaptopodin. Yellow arrows indicate synaptopodin clusters localized inside the dendritic shaft, blue arrows indicate spine-localized synaptopodin. Scale bar = 5 μm.
- H–J Quantification of spine density, synaptopodin clusters and synaptopodin-positive spines as shown in (G) (mean ± SEM, *n* GFP ctrl = 21 cells, *n* cald-GFP = 30 cells; 2 experiments). (H) Spine density is increased in cald-GFP overexpressing neurons compared to the control (in line with 5e). (***P* = 0.0024, unpaired *t*-test). (I) The total number of synaptopodin clusters is not affected by caldendrin overexpression (n.s., unpaired *t*-test). (J) The percentage of synaptopodin-positive spines is increased in cald-GFP overexpressing neurons compared to the control (*****P* < 0.0001, unpaired *t*-test).

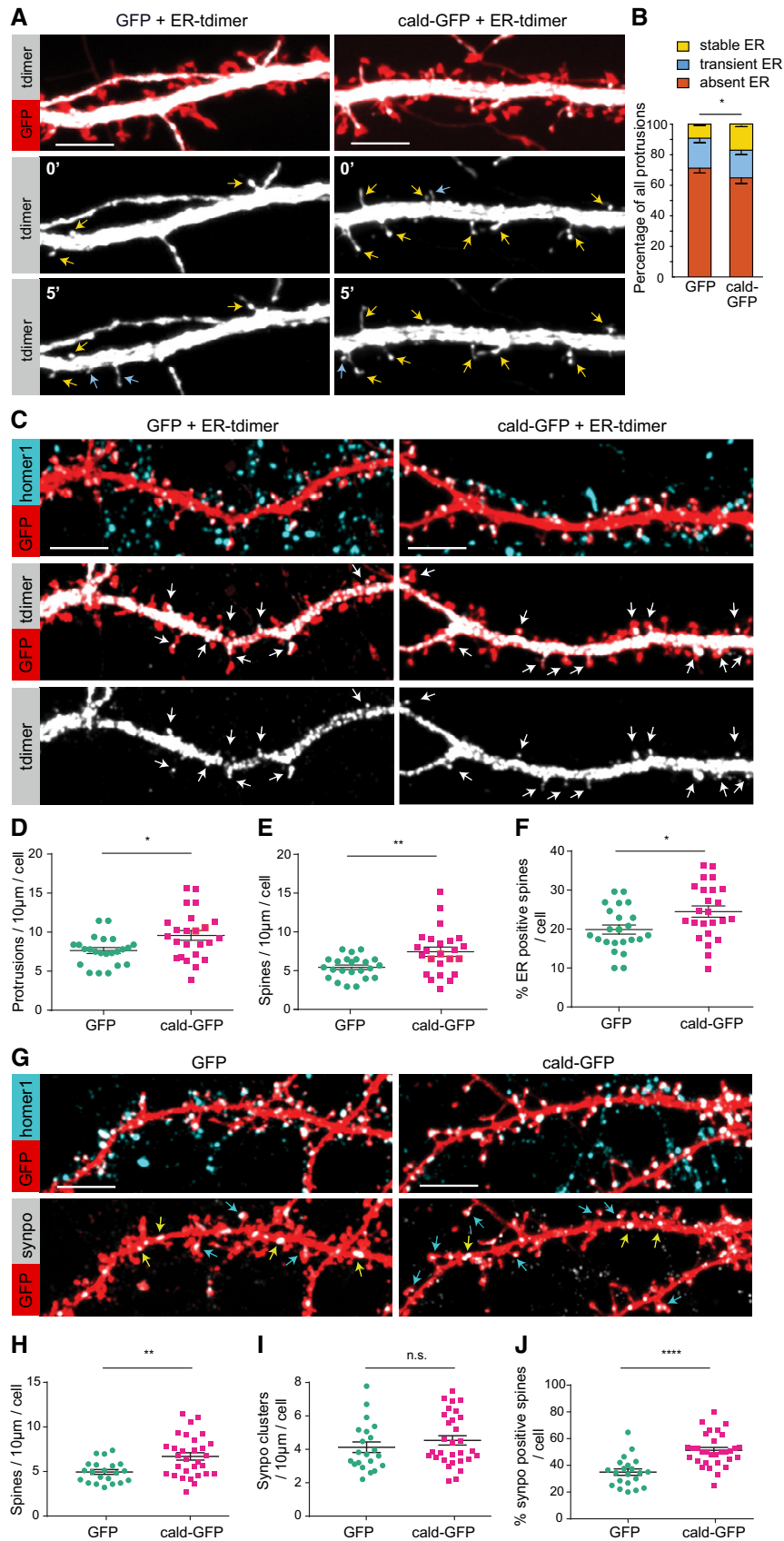


Figure 5.

would affect the localization of the spine apparatus at dendritic spines.

To test this, we expressed caldendrin-GFP (or GFP control) in rat hippocampal neurons and, 8 h prior to fixation, stimulated with 50 μ M bicuculline for 15 min to increase synaptic activity, as induction of long-term potentiation (LTP) of synapses has been shown to boost spine-apparatus formation (Chirillo *et al*, 2019). To visualize synapses and the spine apparatus, neurons were stained for homer1 and synaptopodin, respectively (Fig 5G). Once again, caldendrin-GFP overexpression increased spine density (Fig 5G and H), while it did not affect the overall density of synaptopodin clusters throughout the dendrite (Fig 5I). Interestingly, we found that the percentage of synaptopodin-positive spines had increased from 34.9% in GFP control, to 51.3% in caldendrin-GFP (Fig 5J).

These results are in line with an increase of stably inserted SER observed in the live imaging experiments (Fig 5B). From this we conclude that overexpression of caldendrin increases the dwell-time of SER inside a spine, as well as the percentage of spines that contain a spine apparatus.

Loss of caldendrin in hippocampal neurons destabilizes ER inside dendritic spines

If overexpression of caldendrin stabilizes the ER structures inside dendritic spines, we should observe an opposite effect in the absence of caldendrin. We therefore repeated the same type of ER-live-imaging experiments in hippocampal neurons from caldendrin knockout (cald KO) mice and compared them to their wild-type (cald WT) litter mates, as well as to cald KO neurons overexpressing caldendrin-GFP as a rescue (Fig 6A). We observed that SER-localization to dendritic protrusions was more dynamic and less uniform in KO compared to WT neurons (Figs 6A and EV5A). In both caldendrin WT and KO neurons, a little more than half of the protrusions (59 and 54%, respectively) did not contain any ER during the imaging period (Fig 6B). In KO neurons, the fraction of protrusions that were only transiently visited by the SER was increased significantly (from 23 to 35%), at the expense of the stable ER fraction (Fig 6B). In those protrusions that experienced transient ER visits, the number of multiple ER entries per imaging period was increased in the absence of caldendrin (Fig 6C). Both

of those effects were reversed by overexpression of caldendrin-GFP in KO neurons (Fig 6B and C), with overexpression once again increasing the percentage of “stable” ER over the WT-level (Fig 6B).

In our previous work, we have described the involvement of caldendrin in the stabilization of F-actin in dendritic spines via an interaction with cortactin (Mikhaylova *et al*, 2018). It is possible that this pathway contributed to the observed ER-phenotype. In order to separate the caldendrin-cortactin-F-actin pathway from the caldendrin-myoV-ER pathway, we used chronic exposure to low concentrations of the actin-stabilizing drug jasplakinolide (JPK; 50 nM, 48 h), which we showed previously to be sufficient to counteract the loss of caldendrin with respect to the actin-stabilization pathway (Mikhaylova *et al*, 2018). Of note, neither knockout nor re-introduction of caldendrin, nor JPK treatment significantly affected the total number of dendritic protrusions, that is, the combined occurrence of filopodia and spines (Fig EV5B). Similar to the re-introduction of caldendrin, JPK treatment of KO neurons increased the percentage of protrusions containing “stable” ER significantly, which points toward the involvement of an F-actin-dependent pathway when it comes to the dwell-time of SER inside spines (Fig 6B). Simultaneously, JPK-treatment significantly increased the overall incidence of SER-presence in dendritic protrusions (from 46% in the untreated to 66% in the treated group), with cells still exhibiting a high number of transient SER visits (Fig 6B), as well as the increased number of multiple ER entries (Fig 6C). These results suggest that the caldendrin-mediated dynamics of SER inside dendritic spines are not solely influenced by F-actin stabilization, with myoV activity downstream of caldendrin-mediated pathways being a likely second factor.

Loss of caldendrin decreases spine synapses containing the spine apparatus

As we observed that overexpression of caldendrin in rat neurons led to increased spine apparatus formation in dendritic spines (Fig 5G–J), we asked whether the increase of stable ER in cald KO neurons caused by caldendrin re-introduction and by JPK treatment (Fig 6B) equally results in a higher number of dendritic spines containing the spine apparatus. In other words, does an increased dwell-time of ER

Figure 6. Loss of caldendrin leads to an increased frequency of SER entry and decreased fraction of stable SER in dendritic protrusions of mouse primary hippocampal neurons.

- A 10 min time-lapse imaging of DIV12 wild-type (cald WT), caldendrin knock-out (cald KO), caldendrin knock-out expressing caldendrin-GFP (cald KO + cald-GFP) or caldendrin knock-out treated with jasplakinolide (cald KO + JPK) mouse primary hippocampal neurons, additionally expressing a cell fill (maxGFP) and an ER-marker (ER-tDimer). Yellow arrows indicate protrusions with a stably anchored ER (> 10 min). Blue arrows indicate protrusions that show transient presence of ER. Scale bar = 5 μ m.
- B Quantification of dynamic SER presence in protrusions of cald WT, cald KO, cald KO + cald-GFP, and cald KO + JPK neurons across individual cells, suggesting higher dynamics for cald KO and cald KO + JPK neurons as seen from an increase of protrusions with transiently present ER compared to cald WT neurons, whereas the opposite can be seen for cald KO + cald-GFP (mean \pm SEM, 2-way ANOVA, $***P < 0.001$ for overall interaction, Bonferroni post-tests: $*P < 0.05$ and $**P < 0.01$ for cald WT vs cald KO + cald-GFP, for absent and permanent protrusions, respectively; $***P < 0.001$ for cald WT vs cald KO + JPK for absent protrusions; $***P < 0.001$ for cald KO vs cald KO + cald for permanent protrusions; $**P < 0.01$ for cald KO + cald-GFP vs cald KO + JPK for both absent and permanent protrusions. cald wt, $n = 13$ cells, three experiments; cald KO, $n = 23$ cells, three experiments; cald KO + cald-GFP, $n = 11$ cells, two experiments; cald KO + JPK, $n = 8$ cells, two experiments).
- C Further analysis of the data in (B) for all transiently visited protrusions. In cald WT neurons, roughly 50% of protrusions get visited by an ER only once, while the other half experiences multiple ER entries. This ratio is changed toward multiple ER entries in cald KO neurons, and can be rescued by overexpression of caldendrin-GFP (cald KO + cald), but not by 48 h treatment with 50 nM jasplakinolide (cald KO + JPK). The n of independent experiments, cells and analyzed protrusions is the same as in (B).

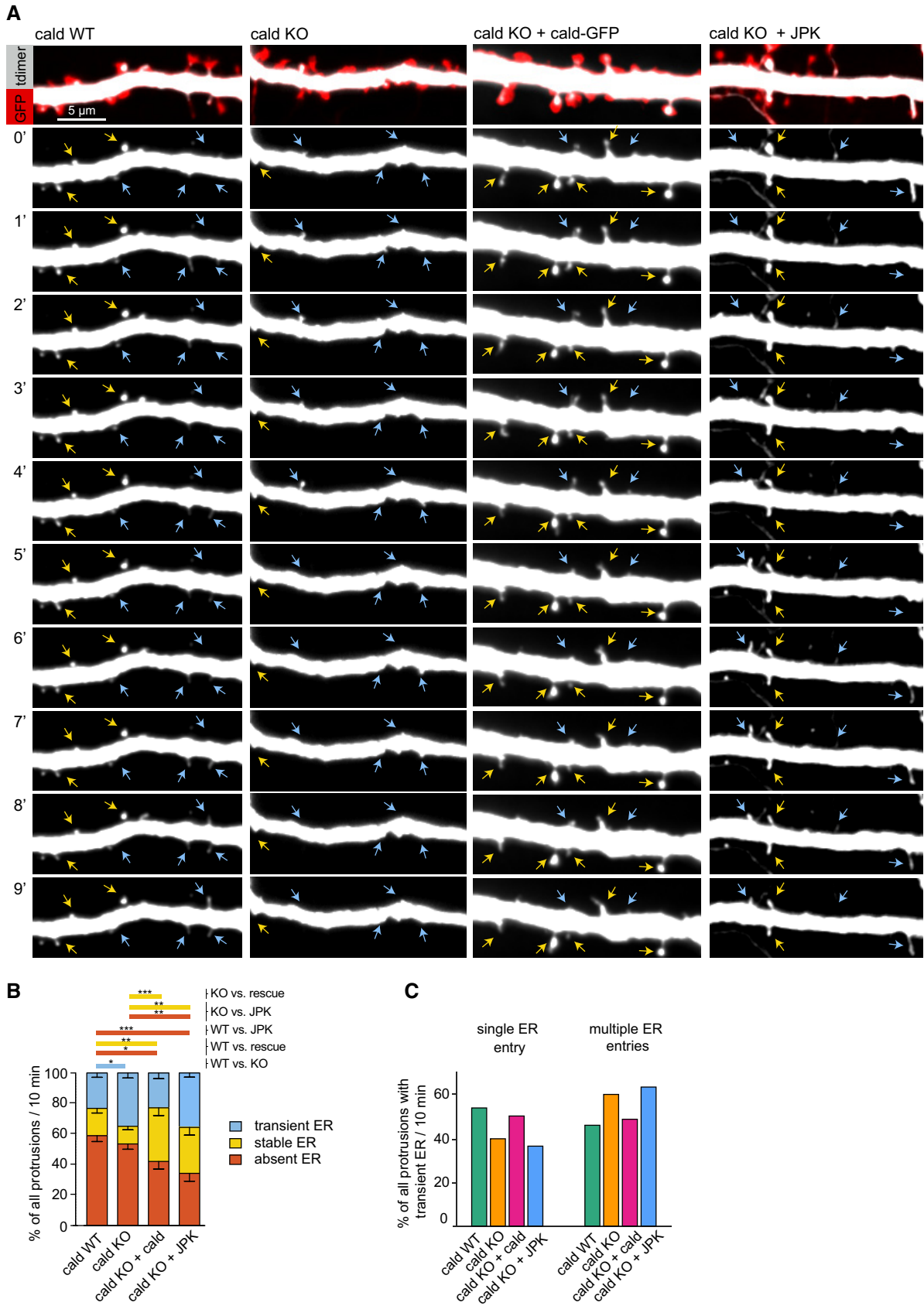


Figure 6.

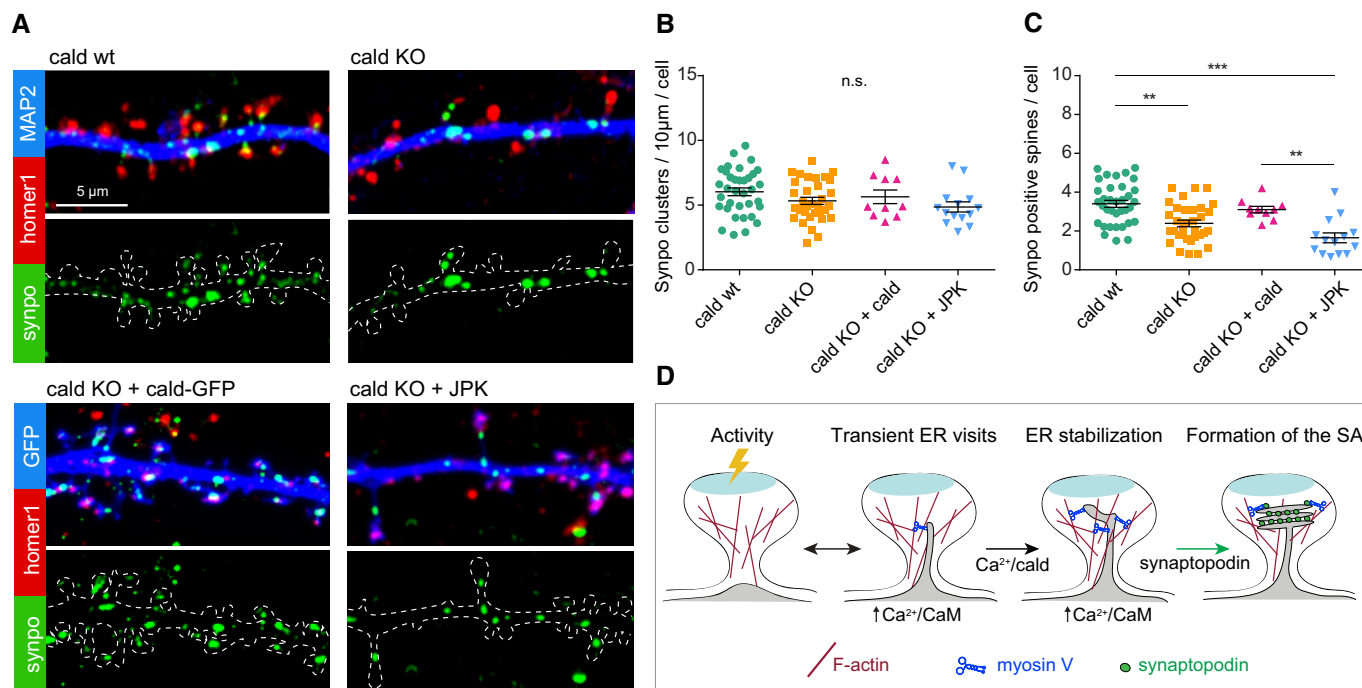


Figure 7. Loss of caldendrin decreases the number of synaptopodin-positive spines, which can be rescued by caldendrin overexpression, but not by the F-actin stabilization.

- A** Representative confocal images of mouse primary hippocampal neurons stained against homer1 and synaptopodin. The groups compared are wild-type (cald WT), caldendrin knock-out (cald KO), caldendrin knock-out expressing caldendrin-GFP (cald KO cald), and caldendrin knock-out treated with jasplakinolide (cald KO JPK). Scale bar = 5 μ m.
- B, C** Quantification of spine density, synaptopodin clusters, and synaptopodin-positive spines as shown in (A) (mean \pm SEM. Kruskal–Wallis test with Dunn’s multiple comparisons post-test. *** P < 0.0001. cald wt n = 34 cells, two experiments; cald KO n = 33 cells, three experiments; cald KO cald n = 10 cells, one experiment; cald KO JPK n = 14 cells, one experiment). (B) The total number of synaptopodin clusters is unaffected by the loss of caldendrin. (C) The number of synaptopodin-positive spines is reduced in cald KO compared to the WT neurons. This phenotype could be rescued by over-expression of caldendrin (cald KO + cald), but not by treatment with JPK (cald KO + JPK).
- D** Model depicting the suggested mechanism of spine apparatus formation. Increased activity results in increased ER visits to the spine, which is mediated by calmodulin-associated myoV. In a subset of spines that are enriched with caldendrin, calcium-dependent myoV-caldendrin interaction transforms the processive motor into an F-actin tether, thereby stabilizing the ER in the spine. Subsequent accumulation of synaptopodin results in the formation of the spine apparatus.

inside dendritic spines, mediated by F-actin stabilization, equal increased spine apparatus formation? To answer this question, we compared the presence of the spine apparatus marker synaptopodin in dendritic spines marked by homer1 in cald KO and cald WT neurons, as well as cald KO neurons transfected with caldendrin-GFP or treated with 50 nM JPK for 48 h (Fig 7A). We found that, while the lack of caldendrin did not affect the overall number of synaptopodin clusters (Fig 7B), the number of dendritic spines containing the spine apparatus was significantly lower compared to wild-type neurons (Fig 7C). This phenotype could be rescued by the overexpression of caldendrin, but not by JPK treatment (Fig 7B and C). Notably, while JPK did not affect the overall number of synaptopodin clusters (Fig 7B), the spine localization was strongly reduced (Fig 7C), despite the increase in ER-dwell-time observed under the same conditions (Fig 6B).

We therefore conclude that there are two separate pathways at play here that involve caldendrin: one that increases dwell-time of SER inside dendritic spines dependent on F-actin stabilization (via caldendrin-cortactin-actin), and another that stimulates SA formation, and requires coordinated action of caldendrin and myoV (Fig 7D).

Discussion

In this study, we aimed to decipher how the modalities of Ca²⁺-sensing in myoV influence its processivity and stalling behavior, which is instrumental for the proper synaptic targeting of SER to a subset of active dendritic spines in hippocampal neurons.

Although it is well accepted that Ca²⁺/CaM regulates the active vs. inactive conformation and processivity of myoV (and myoVI), there are surprisingly few studies addressing the exact role of Ca²⁺ in regulation of unconventional myosins in living cells (Krementsov *et al*, 2004; Wang *et al*, 2008). Here, we found through a MS screen that another brain-specific Ca²⁺-binding protein, caldendrin, associates with various myosin family members, including myoVa, Vb, and myoVI, in a Ca²⁺-dependent manner. The moderate Ca²⁺-binding affinity of the protein (Reddy *et al*, 2014) would restrict Ca²⁺-dependent interactions of caldendrin to compartments with steep Ca²⁺-gradients, such as dendritic spines. Additionally, in contrast to the diffusely distributed CaM, caldendrin is enriched in big and mature spines that are expected to experience frequent synaptic inputs with large Ca²⁺-transients. Known roles of caldendrin include activity-dependent stabilization of F-actin via interaction with

cortactin, regulation of IP₃Rs present at the ER, as well as regulation of L-type calcium channels and synapse-to-nucleus communication via the messenger-protein Jacob (Tippens & Lee, 2007; Dieterich *et al*, 2008; Li *et al*, 2013; Mikhaylova *et al*, 2018). Larger mushroom-like spines are stable over time, have a stronger synaptic connection, and frequently contain SER. MyoV has been shown to be implicated in the activity-dependent targeting of SER upon induction of synaptic plasticity (Kneussel & Wagner, 2013; Perez-Alvarez *et al*, 2020). We therefore asked whether the interaction between caldendrin and myoV isoforms could have functional consequences for targeting and stabilization of the ER-derived structures in dendritic spines.

To first identify the binding interface, we performed co-immunoprecipitation assays with various truncation constructs of both proteins. Ca²⁺-dependent accessibility of caldendrin is mediated by its C-terminal domain, which masks the N-terminus in the absence of Ca²⁺. However, we still observed a Ca²⁺-dependent interaction between the isolated caldendrin N-terminus and myoV, which suggested that another calcium-sensing modality might be involved.

By further narrowing down the binding region, we found that caldendrin specifically recognizes a 49 amino-acid fragment of myoV containing part of the lever arm with the first IQ-motif and part of the motor domain. Again, we found that the binding of caldendrin to this peptide was mediated by the caldendrin N-terminus. Despite its structural similarity to CaM, to our surprise the isolated caldendrin C-terminus showed no interaction with the IQ1-containing myosin peptide. An attempt to narrow down the interaction site on the caldendrin N-terminus failed, as none of the tested truncations of the N-terminus retained the ability to interact with myosin. Although the N-terminus is mostly unfolded, our experimental data suggest a clear nonrandom behavior in binding to myoV. Based on what is known about the binding behavior of unstructured proteins, we speculate that the unstructured caldendrin N-terminus might partially collapse upon binding to myoV, thereby inducing the formation of ordered structure, which is referred to as “folding-upon-binding” (Bowler, 2012; Mollica *et al*, 2016). Such a mechanism might require the presence of the N-terminus as a whole, or several amino acid residues from different regions within the N-terminus, and could explain the loss of interaction when the N-terminus was truncated. To show this experimentally in a future study, one could try cocrystallization of caldendrin with the myoVa IQ1-containing peptide.

The fact that the caldendrin and IQ1-CaM-binding sites on myoV are either in close proximity or possibly even overlap carries interesting implications for the effect of caldendrin binding on myoV activity. IQ1-CaM was shown to be responsible for the observed stimulation of actin-activated ATPase activity of myoV by micromolar Ca²⁺: in its inactive state, myoV is in an auto-inhibited, folded conformation in which the C-terminal cargo-binding domain is in contact with the N-terminal motor domain (Sellers *et al*, 2008; Wang *et al*, 2008). Ca²⁺-induced conformational change of IQ1-CaM can break the interaction between myoV motor and cargo domain, thus activating motor function (Lu *et al*, 2012; Shen *et al*, 2016). A possible explanation for the observed Ca²⁺-sensitivity of the caldendrin-myoV interaction could therefore be the described conformational change in IQ1-CaM upon binding of Ca²⁺ (Lu *et al*, 2012; Shen *et al*, 2016). In addition to that, Ca²⁺ binding to IQ1-CaM was shown to

not only cause significant changes to the lever arm, but also propagated changes that extend into the motor domain (Trybus *et al*, 2007), which might explain the observed reduction of myoV velocity between IQ1-Ca²⁺/CaM and IQ1-apoCaM (Krementsov *et al*, 2004). It is therefore likely that caldendrin binding closely to the IQ1-CaM interface will affect myoV motor function.

To investigate this in more detail, we performed native MS measurements including CaM, caldendrin, and the identified 49 amino-acid fragment of myoVa in different combinations. Here, again we could demonstrate direct interaction of Ca²⁺-bound caldendrin to myoV peptide.

Interestingly, we observed binding of CaM to the IQ1-containing peptide only when CaM was fully saturated with four Ca²⁺-ions, rather than partially saturated or Ca²⁺-free. There are several papers reporting that CaM is strongly attached to IQ1 of myoVa *in vitro* in the absence of Ca²⁺, however they have not looked directly at the Ca²⁺ ion occupation of CaM (Nascimento *et al*, 1996; Krementsov *et al*, 2004; Nguyen & Higuchi, 2005; Shen *et al*, 2016). We explain this apparent discrepancy by the differences in experimental procedures. To the best of our knowledge, current literature shows that myoV fully decorated with CaM, purified from tissue or cultured cells, stays strongly associated with all of its CaM light chains in Ca²⁺-free buffer, while some of them detach in high Ca²⁺ concentrations that is, CaM already bound to myoVa does not detach in EGTA buffer possibly due to ability of CaM to retain Ca²⁺ in myosin-bound form, while it is questionable whether Ca²⁺-free apo-CaM can actually associate *de novo* with IQ1 of myoVa. There is an interesting study showing re-activation of myosin activity in an *in vitro* gliding assay, after myosin has been inactivated by loss of CaM in high Ca²⁺ concentrations, by “removing Ca²⁺ from the solution in the presence of CaM” (Nguyen & Higuchi, 2005). However, unfortunately the buffer composition during this incubation step was not specified, so no statements can be made about the Ca²⁺-occupancy of the CaM in this assay. Further, it is likely that in the above-mentioned assay, what the authors observed was CaM detaching from and re-attaching to IQ2 (Koide *et al*, 2006), whereas we are looking at CaM binding to IQ1. In our experimental setup, we added exogenous CaM purified from bacteria to the purified myosin IQ1-containing peptide, either in Ca²⁺-free or 200 μM Ca²⁺-containing ammonium acetate solution, so what we see is mostly *de-novo* association. In that case, we observed no new binding of CaM to the myosin peptide. Finally, when we combined all three components, CaM, caldendrin, and the myoVa peptide, native MS showed both Ca²⁺ sensors binding to the myoV fragment individually, while no complex containing all three proteins could be seen. Along the same line, *in vitro* competition pull downs from cell lysate with CaM and caldendrin indicated that, in the presence of Ca²⁺, caldendrin can replace CaM at IQ1. Importantly, full decoration of the lever-arm with CaM is a known prerequisite for processive myoV motor function, as detachment of one or several CaMs leads to destabilization of the lever arm, which is then no longer able to translate the force generated by ATP hydrolysis into processive motility (Koide *et al*, 2006; Trybus *et al*, 2007). It is possible that potential displacement of IQ1-CaM by caldendrin would affect myoVa processivity in a similar way. Here, we further showed that the processivity of the myoVa motor is generally inhibited by the presence of caldendrin in a reconstituted *in vitro* gliding assay. It is known that in a gliding assay setup, myosin motors that are attached to the glass surface

are forced into an “open” conformation, preventing formation of the auto-inhibited state (Krementsov *et al*, 2004). We can therefore conclude that the inhibitory effect that caldendrin has on myoVa affects the motor in its open and active conformation.

As conformational changes of CaM and/or the myoV lever arm can extend to the motor domain (Trybus *et al*, 2007), we reasoned that the observed inhibition of myoVa processivity in the gliding assay could be due to caldendrin affecting myoVa interaction with F-actin. However, using an *in vitro* F-actin cosedimentation assay and an inducible motor-cargo assay in COS7 cells, we did not find any evidence that caldendrin negatively affects myoV binding to F-actin. Alternatively, caldendrin could exert its inhibitory function by “locking” the lever arm in place, preventing myoV from stepping forward, but without displacing it from F-actin. This would explain both results from the *in vitro* gliding assay and the inducible motor-cargo assay.

The invasion of SER into dendritic spines is one example of a cellular process where controlled stop-and-go behavior of myoV plays an instrumental role. In a recent study, it has been shown that transient SER spine entries are not random but target highly activated spines (Perez-Alvarez *et al*, 2020). In another study, LTP-driven transformation of the SER into a spine apparatus has been reported (Chirillo *et al*, 2019). Adding to that, in our previous work, we have shown that myoV activity is required for synaptic accumulation of synaptopodin and formation of the spine apparatus (Konietzny *et al*, 2019). Based on this, we hypothesized that the Ca²⁺-dependent interplay of CaM, caldendrin, and myoV represents a core mechanism of recruitment and stabilization of SER in dendritic spines.

While performing live imaging of SER-spine-entry in hippocampal neurons, we observed that overexpression of caldendrin led to an increase of stable SER, while the dynamics of transient SER visits were unchanged compared to the control. As it was recently shown, a high percentage of spines that show stably inserted SER actually contain a spine apparatus (Perez-Alvarez *et al*, 2020). Indeed, caldendrin overexpression significantly increased the spine-localization of synaptopodin, indicating that we were looking at increased spine apparatus formation.

In agreement with the overexpression experiments, we found that caldendrin knock out neurons exhibited fewer dendritic protrusions with stable SER, while a higher number of spines experienced transient SER visits. This effect was rescued by the re-introduction of caldendrin. Similarly, the percentage of dendritic spines containing the spine apparatus was significantly reduced in caldendrin knockout and could be rescued by caldendrin overexpression.

The observed effects could be explained by caldendrin either stabilizing spinous F-actin or regulating myoV motor function. Since we could not pin-point individual amino acid residues of caldendrin involved in the interaction, we were unable to generate point-mutants that disrupt binding to myoV specifically without interfering with other interaction partners. When used in rescue-experiments in caldendrin knockout neurons, such a mutant could have been a direct proof of the proposed caldendrin-myosin-ER-spine apparatus pathway. As an alternative strategy, in order to discriminate between these two possibilities, we subjected caldendrin knockout neurons to chronic exposure of low concentrations of the actin-stabilizer JPK. Although JPK treatment also increased the percentage of spines containing ER stably present over 10 min imaging time, it did not rescue the low number of synaptopodin-

positive spines. This means that, in the absence of caldendrin, F-actin stabilization alone was not sufficient to rescue synaptic targeting of the spine apparatus. We conclude that, while the caldendrin-mediated increase in dwell-time of SER inside dendritic spines could be explained by both the caldendrin-myoV-ER anchoring and by the caldendrin-cortactin-F-actin-stabilization pathway (Mikhaylova *et al*, 2018), the spine apparatus targeting relies on the caldendrin-myosin interaction. It is important to note that caldendrin can only be one of several factors that determine whether an ER gets long-term anchored inside a spine. Otherwise, spines of hippocampal neurons from caldendrin knockout mice should be completely devoid of long-term inserted ER, which we have shown is not the case. The above-described mechanism is probably specific for highly plastic neurons in the telencephalon where synaptopodin and caldendrin are strongly expressed (Mundel *et al*, 1997; Laube *et al*, 2002). Interestingly, in cerebellar Purkinje neurons (PNs), essentially every single dendritic spine contains a stably anchored ER protrusion, which critically depends on myosin V (Wagner *et al*, 2011). As PN do not express caldendrin (Laube *et al*, 2002; Kim *et al*, 2014) other caldendrin-independent mechanisms of spine-ER-anchoring must exist in this cell type. Of note, PNs are also lacking the synaptopodin protein and do not form the spine apparatus (Deller *et al*, 2003).

Based on all the data presented here, as well as previously published data showing that myoV plays a role in the synaptic enrichment of synaptopodin, and thereby spine apparatus formation (Konietzny *et al*, 2019), we propose the following model: As myoV processively transports SER into recently activated spines, once it reaches the spine head where caldendrin is enriched, Ca²⁺/caldendrin will replace Ca²⁺/CaM from IQ1 and inhibit further motility. Importantly, it does not dissociate myoV from F-actin, but rather locks it in place to function as a tether. Ca²⁺ concentrations are highest in the heads of large dendritic spines that usually experience high frequency synaptic stimulation, for instance during LTP. As caldendrin has to compete with other Ca²⁺-binding proteins for Ca²⁺ ions, it is most likely to become activated in the confined spine head, and to a lesser extent in the spine neck or dendritic shaft (Raghuram *et al*, 2012; Reddy *et al*, 2014). Subsequent accumulation of synaptopodin will allow the emergence of a stable spine apparatus organelle. It is possible that in a very similar way, the caldendrin-myoV-dependent tethering of synaptopodin can further facilitate this process (Fig 7D).

What is the role of SER inside dendritic spines? In recent work, it has been proposed that the presence of SER correlates with LTP-like activity of individual spines, and that it is involved in the depotentiation of spines in an mGluR1-dependent manner (Holbro *et al*, 2009; Perez-Alvarez *et al*, 2020). SER contains IP₃Rs, which are important for the long-term depression (LTD) and downscaling of over-activated spines (Nakamura *et al*, 1999; Holbro *et al*, 2009; Segal & Korkotian, 2014). Interestingly, caldendrin binds IP₃R and decreases its sensitivity for IP₃ (Li *et al*, 2013). This could provide a mechanism to fine-tune the sensitivity of caldendrin- and SER-positive spines to LTP- and LTD-like stimuli. Indeed, in our previous work we found that caldendrin knockout mice fail to form a stable LTP in CA1-Schaffer collaterals. This effect could be partially rescued by stabilization of actin filaments with JPK during the LTP induction (Mikhaylova *et al*, 2018). It is possible that the deficiency in synaptic targeting of the spine apparatus mediated by caldendrin

and myoV interaction was another limiting factor for the maintenance of synaptic potentiation.

Overall, we propose a Ca^{2+} -sensitive module comprising myoV, CaM, and caldendrin as a key ER delivery mechanism that is operational in a subset of dendritic spines and contributes to the diversification and specification of excitatory glutamatergic synapses. Future studies will elucidate whether the same rules apply to the synaptic targeting of other myoV cargoes, such as mRNA granules or recycling endosomes.

Materials and Methods

Animals

Wistar Unilever HsdCpb:WU (Envigo) rats and caldendrin knockout mice (Mikhaylova *et al.*, 2018) were used in this study. All animal experiments were carried out in accordance with the European Communities Council Directive (2010/63/EU) and the Animal Welfare Law of the Federal Republic of Germany (Tierschutzgesetz der Bundesrepublik Deutschland, TierSchG) approved by the local authorities of Sachsen-Anhalt/Germany (reference number 42502-2-987IfN and 42502-2-1264 LIN, TV 42502-2-1009 UniMD) or of the city-state Hamburg (Behörde für Gesundheit und Verbraucherschutz, Fachbereich Veterinärwesen) and the animal care committee of the University Medical Center Hamburg-Eppendorf.

Primary neuronal culture and transfections

Primary hippocampal rat cultures were prepared essentially as described previously (Kapitein *et al.*, 2010). In brief, hippocampi were dissected from E18 embryos, treated with trypsin (0.25%, Thermo Fisher Scientific) for 10 min at 37°C, physically dissociated by pipetting through a syringe, and plated on poly-L-lysine (Sigma-Aldrich, #P2636)-coated glass coverslips (18 mm) at a density of 40,000–60,000 cells per 1 ml in DMEM (Gibco, #41966-029) supplemented with 10% fetal calf serum (Gibco, #10270) and antibiotics (Thermo Fisher Scientific, #15140122). After 1 h, the plating medium was replaced by BrainPhys neuronal medium supplemented with SM1 (Stem Cell kit, #5792) and 0.5 mM glutamine (Thermo Fisher Scientific, #25030024). Cells were grown in an incubator at 37°C, 5% CO_2 , and 95% humidity.

Primary hippocampal neuronal cultures from caldendrin wild type and knock-out mice were prepared as described previously (Mikhaylova *et al.*, 2018). In brief, hippocampi were dissected from male and female P0 mouse pups and after 15 min treatment with trypsin at 37°C cells were physically dissociated by pipetting through a syringe. Neurons were plated on glass coverslips (18 mm) coated with poly-L-lysine (Sigma-Aldrich) at a density of 30,000–80,000 cells per ml in DMEM (Gibco) supplemented with 8% FCS and 1% penicillin/streptomycin. Following attachment, mouse neuronal cultures were kept in Neurobasal medium (NB; Gibco) supplemented with 2 mM glutamine, and 1x B27 supplement (Gibco), at 37°C, 5% CO_2 , and 95% humidity.

Primary cultures were transfected with lipofectamine 2000 (Thermo Fisher Scientific) according to the manufacturer's instructions. Rat neurons were transfected between DIV15–17, mouse neurons were transfected between DIV10–11. Experiments on transfected neurons were performed 24 h after transfection. For cotransfection of

plasmids, the ratios of different constructs were optimized individually, and optionally by addition of an “empty vector” (pcDNA3.1) to tune expression levels. Before transfection, the conditioned neuronal medium was removed from the cells and kept at 37°C. Neurons were transfected in BrainPhys medium lacking SM1 (rat cultures) or in Neurobasal medium lacking B27 (mouse cultures) by incubation in the transfection mixture for 45 min–1.5 h. After transfection, the medium was exchanged back to the conditioned medium.

For fixed imaging of ER spine localization together with synaptopodin, 16 h after transfection and 8 h before fixation, neurons were transferred into medium containing 50 μM Bicuculline (Tocris) for 15 min to increase synaptic activity, and then back to their conditioned medium.

For live or fixed imaging of caldendrin knock-out neurons treated with jasplakinolide, the drug was added to a final concentration of 50 nM to the culture medium for a time span of 48 h before imaging or fixation.

Culturing and transfection of cell lines

HEK293T cells (DSMZ, ACC 635) and COS7 cells (ATCC, CRL-1651) were maintained in full medium consisting of Dulbecco's modified Eagle's medium (DMEM; GIBCO, Thermo Fisher) supplemented with 10% fetal calf serum (FCS), 1x penicillin/streptomycin, and 2 mM glutamine at 37°C, 5% CO_2 , and 95% humidity. For the expression of biotinylated proteins, cells were grown in full medium made with a 50% DMEM, 50% Ham's F-10 Nutrient Mix (GIBCO, Thermo Fisher) mixture. HEK293T cell transfections were done using MaxPEI 25K (Polysciences) in a 3:1 MaxPEI:DNA ratio according to the manufacturer's instructions. Transfected HEK293T cells were harvested 18–24 h after transfection. The cells were washed 1x in cold TBS, resuspended in 2 ml of TBS, and pelleted for 3 min at 1,000 g. The cell pellet was lysed in 500 μl of extraction buffer (20 mM of Tris pH 8, 150 mM of NaCl, 1% Triton-X-100, 5 mM of MgCl_2 , complete protease inhibitor cocktail [Roche]), kept on ice for 30 min, and centrifuged for 15 min at 14,000 g. The supernatant (cleared lysate) was then further used for experiments.

COS7 cells were plated and imaged in 35-mm glass-bottom μ -dishes (Ibidi, #81156) or on uncoated glass coverslips. They were transfected using FuGene HD (Promega, #E2311) in a 3:1 FuGene:DNA ratio according to the manufacturer's instructions. Transfected COS7 cells were imaged 18–24 h after transfection. During image acquisition, rapalog (A/C Heterodimerizer, TaKaRa, #635056) was added at a final concentration of 100 nM.

Immunoblotting

For immunoblot analysis, samples were either taken up in commercial Bolt LDS sample buffer (Invitrogen), or self-made SDS sample-buffer (4x stock: 250 mM of Tris-HCl, pH 6.8, 8% (w/v) SDS, 40% (v/v) glycerol, 5% (v/v) β -mercaptoethanol, 0.004% bromophenol blue, pH 6.8) as specified. In general, samples were boiled at 98°C for 10–15 min, run on 4–20% acrylamide gradient gels, and blotted on PVDF membranes in blotting buffer (192 mM of glycine, 0.1% (w/v) SDS, 15% (v/v) methanol, 25 mM of Tris-base, pH 8.3). After blocking the membranes in 5% skim milk in Tris-buffered saline (TBS, 20 mM of Tris pH 7.4, 150 mM of NaCl, 0.1% Tween-20), membranes were incubated with primary antibodies diluted in

TBS-A (TBS pH 7.4, 0.02% sodium-azide) overnight at 4°C. Corresponding HRP-conjugated secondary antibodies or HRP-Streptavidin were applied for 1.5 h at RT in 5% skim milk in TBS. The membranes were imaged on a ChemoCam imager (Intas).

Biotin-streptavidin pull-down experiments

HEK293T cells were cotransfected with HA-BirA and either Caldendrin-pEGFP-bio, or pEGFP-bio (control vector) and harvested on the next day as described above. Magnetic Streptavidin M-280 Dynabeads (Invitrogen) were washed 3× in washing buffer (20 mM of Tris pH 8, 150 mM of KCl, 0.1% Triton-X 100), blocked in 3% chicken egg albumin (Sigma) for 40 min at RT, and again washed 3× in washing buffer. The cleared cell lysate was added to the blocked beads and incubated at 4°C on a rotator overnight. After the incubation period, the beads were washed 2× with low salt washing buffer (100 mM of KCl), 2× in high salt washing buffer (500 mM of KCl) and again 2× in low salt washing buffer. For preparation of whole mouse brain extract, 9 ml of lysis buffer (50 mM of Tris-HCl pH 7.4, 150 mM of NaCl, 0.1% SDS, 0.2% NP-40, complete protease inhibitor cocktail [Roche]) were added per 1 g of tissue weight, and the tissue was lysed using a Dounce homogenizer. The lysate was cleared first for 15 min at 1,000 g, and the supernatant was again centrifuged for 20 min at 15,000 g to obtain the final lysate. The washed beads were then combined with 1 ml of the cleared mouse brain lysate and incubated for 1 h at 4°C on a rotator. The beads were divided into 2× samples, and incubated with mouse brain lysate that was either substituted with 2 mM of EGTA or with 0.5 mM of CaCl₂ and 1 mM of MgCl₂. After the incubation period, the beads were washed 5× in washing buffer and resuspended in Bolt LDS sample buffer (Invitrogen) for subsequent SDS-PAGE and MS or western blot analysis. For mass-spectrometric analysis, the samples were separated on a commercial Bolt Bis-Tris Plus Gel (Invitrogen) and the intact gel was sent to Erasmus MC Proteomics Center, Rotterdam, for MS analysis (see below).

Co-immunoprecipitation from HEK293T cells

HEK293T cells were transfected with the respective GFP-tagged myosin construct and either with tagRFP-tagged caldendrin or tagRFP as a control, and harvested as described above. Forty-five microliters of the cleared lysate were taken as an “input” sample. The remaining SN was split into 2× 200 µl, distributed into separate tubes and substituted with either 2 mM EGTA or 0.5 mM CaCl₂ and 1 mM MgCl₂. GFP-trap beads (Chromotek) were washed 2× in extraction buffer and an equivalent of 7 µl of slurry was added to the tubes containing the cell lysates. The beads were then incubated on a rotor at 4°C for 2–4 h. After the incubation period, the beads were washed 3× in washing buffer (20 mM of Tris, 150 mM NaCl, 0.5% Triton-X-100, complete protease inhibitor cocktail [Roche]) that was either substituted with 2 mM of EGTA or 0.5 mM of CaCl₂ and 1 mM of MgCl₂. The beads were then taken up in 30 µl of SDS sample-buffer for SDS-PAGE.

Pull down of purified myosin with recombinant caldendrin

HEK293T cells were transfected with the respective GFP-tagged myosin constructs and either with tagRFP-tagged caldendrin or

tagRFP as a control, and harvested as described above. The cleared lysate was incubated with an equivalent of 7 µl of GFP-trap slurry (Chromotek) for 6 h at 4°C on a rotor, then the beads were washed 3× with washing buffer (20 mM of Tris, 150 mM of NaCl, 0.5% Triton-X-100, complete protease inhibitor cocktail [Roche]), blocked with washing buffer supplemented with 5% BSA, and then divided into 4 equal samples. Each sample was incubated with washing buffer supplemented with 100 nM of either purified, recombinant wild-type caldendrin, or a caldendrin calcium-binding mutant (D243A, D280A, (Mikhaylova *et al*, 2018)), in the presence or absence of 2 mM of EGTA or 100 µM of CaCl₂. After the incubation period, the beads were washed 3× in washing buffer (20 mM of Tris, 150 mM of NaCl, 0.5% Triton-X-100, complete protease inhibitor cocktail [Roche]) that was either substituted with 2 mM of EGTA or 100 µM of CaCl₂. The beads were then taken up in 30 µl of SDS sample-buffer for SDS-PAGE.

Co-immunoprecipitation of GFP-myoVa peptide with tagRFP-caldendrin and recombinant CaM

Separate batches of HEK293T cells were transfected with either GFP-tagged myoVa peptide, tagRFP-caldendrin, or tagRFP only, and harvested as described above. The cleared lysate of GFP-myoVa-peptide was supplemented with 100 µM of recombinant CaM, and the sample was separated into two equal parts, to which the cleared cell lysate from either tagRFP-caldendrin-transfected or tagRFP-only transfected cells was added. Each of those two samples was divided into two samples once again, and either 0.5 mM of CaCl₂ + 1 mM of MgCl₂ or 2 mM of EGTA were added. Each of the eight samples was then incubated with an equivalent of 4 µl of GFP-trap slurry (Chromotek) for 3 h at 4°C on a rotor, then the beads were washed 3× with washing buffer (20 mM of Tris, 150 mM of NaCl, 0.5% Triton-X-100, complete protease inhibitor cocktail [Roche]) that was either substituted with 2 mM EGTA or 100 µM of CaCl₂ and taken up in 30 µl of SDS sample-buffer for SDS-PAGE.

Mass spectrometry and data analysis

Pull-down samples were separated on a commercial Bolt Bis-Tris Plus Gel (Invitrogen) and analyzed at the Erasmus MC Proteomics Center, Rotterdam. Briefly, SDS-PAGE gel lanes were cut into 1-mm slices using an automatic gel slicer. Per sample, 8–9 slices were combined and subjected to in-gel reduction with dithiothreitol, alkylation with iodoacetamide, and digestion with trypsin (Thermo Fisher Scientific, TPCK treated), essentially as described by (Wilm *et al*, 1996). Nanoflow LCMS/MS was performed on an EASY-nLC 1000 Liquid Chromatograph (Thermo Fisher Scientific) coupled to an Orbitrap Fusion™ Tribrid™ Mass Spectrometer (Thermo Fisher Scientific) operating in positive mode and equipped with a nanospray source. Peptide mixtures were trapped on a nanoACQUITY UPLC C18 column (100 Å, 5 µm, 180 µm × 20 mm, Waters). Peptide separation was performed on a ReproSil C18 reversed phase column (Dr Maisch GmbH; 20 cm × 100 µm, packed in-house) using a linear gradient from 0 to 80% B (A = 0.1% formic acid; B = 80% [v/v] acetonitrile, 0.1% formic acid) in 60 min and at a constant flow rate of 200 nl/min. Mass spectra were acquired in continuum mode; fragmentation of the peptides was performed in data-dependent mode.

Mass spectrometric raw data were analyzed using the MaxQuant software suite (version 1.5.4.1) for identification and relative quantification of peptides and proteins. A false discovery rate (FDR) of 0.01 for proteins and peptides, and a minimum peptide length of 6 amino acids were required. The Andromeda search engine was used to search the MS/MS spectra against the *Homo sapiens* and *Mus musculus* Uniprot databases (release July 2016) concatenated with the reversed versions of all sequences and a contaminant database listing typical background proteins. A maximum of two missed cleavages were allowed. MS/MS spectra were analyzed using MaxQuant's default settings for Orbitrap and ion trap spectra. The maximum precursor ion charge state used for searching was 7 and the enzyme specificity was set to trypsin. Further modifications were Cysteine carbamidomethylation (fixed) as well as Methionine oxidation (variable). The minimum number of peptides for positive protein identification was set to 2. The minimum number of razor and unique peptides was set to 1. Only unique and razor nonmodified, methionine oxidized, and protein N-terminal-acetylated peptides were used for protein quantitation.

Analysis of mass spectrometry data

Identified peptides (see Dataset EV1) were manually curated by removing ambiguous peptides if more than one of their associated proteins also had other unique peptides. Sample variability of the amount of "bait" (caldendrin-GFP or GFP alone) was taken into account by summing the intensities of the highest (> 60th percentile) intensity GFP-peptides in each sample and using this as a relative correction factor for all other peptide intensities in that sample. Intensity ratios of proteins with at least $n = 5$ associated peptides in this curated list were then calculated according to. All protein intensity data were manually verified to accurately reflect the calculated ratio.

$$\frac{\sum_1^n I_{cald+Ca^{2+}}(n) - \sum_1^n I_{GFP+Ca^{2+}}(n)}{\sum_1^n I_{cald+EGTA}(n) - \sum_1^n I_{GFP+EGTA}(n)}$$

Circular dichroism spectroscopy

To estimate the folding and solvent effects on the MyoIQ1 peptide secondary structure, circular dichroism spectroscopy was performed on a Chirascan circular dichroism spectrometer (Applied Photophysics; (Zhong & Johnson, 1992; Kelly *et al*, 2005; Li *et al*, 2011). Prior to the measurement of CD spectra, a single 0.8 mg aliquot of the lyophilized myoVa IQ1-containing peptide was dissolved in ultrapure water to a stock concentration of 2.5 mg/ml. Subsequently, the peptide was diluted to 0.1 mg/ml with ultrapure water and CD spectra including blank were recorded from 260 to 180 nm in a 1 mm quartz cuvette (0.5 nm step size, 3 s/point, 25 μ s sampling time, $T = 20.0 \pm 0.3^\circ\text{C}$, bandwidth = 1 nm, three repeats). We observed a time-dependent increase of α -helical signals (190/205 and 222 nm band) from CD spectra of freshly dissolved peptide, suggesting that the peptide requires some time (30–60 min) to adopt its finally folded state. Therefore, the same timeline was used for the native mass spec experiments. To estimate potential solvent effects on the peptide secondary structure, CD spectra were additionally recorded in 150 mM of ammonium acetate (NH_4OAc) solution (pH 7.4). Here, a 470 μM of stock solution of previously desalted myoVa IQ1-containing peptide was diluted to

$\sim 16.3 \mu\text{M}$ (0.1 mg/ml) in NH_4OAc solution. CD spectra were recorded as outlined above with the spectral range limited to 260–200 nm due to high absorbance of ammonium acetate.

Acquired raw peptide and buffer CD spectra were averaged, Savitzky-Golay smoothed (polynomial order = 2, 15 point window) and subsequently subtracted. The data were converted to the mean residue ellipticity $[\theta]$ as described elsewhere (Greenfield, 2007). To estimate individual secondary structure contents of the peptide, single spectrum analysis (180–250 nm for H_2O and 200–250 nm for NH_4OAc buffer; scaling of spectral amplitude = 1.65) was performed using the BeStSel server (Micsonai *et al*, 2018).

Native mass spectrometry and data analysis

Both full-length caldendrin and CaM as well as the synthetic myoVa peptide were buffer exchanged into 150 mM of aqueous ammonium acetate solution (pH 7.4), which acts in native MS as a volatile buffer surrogate (Hedges *et al*, 2013). While CaM was twice passed through a Bio-Spin P-6 gel filtration spin column (6 kDa cut-off, Bio-Rad), caldendrin and the myoVa peptide were buffer exchanged through five cycles of tenfold dilution and re-concentration using centrifugal concentrators Vivaspin 500 (10 kDa cut-off, Sartorius) or Amicon Ultra 0.5 ml (3 kDa cut-off, Merck/Millipore), respectively. Following buffer exchange, proteins were introduced into an Orbitrap Q Exactive UHMR mass spectrometer (Thermo Scientific) via static nanoelectrospray ionization from in-house prepared gold-coated borosilicate glass capillaries Kwik-Fil 1B120F-4 (World Precision Instruments) essentially as described before (Krichel *et al*, 2021). Proteins were sprayed and analyzed at 8.5 μM concentration in ammonium acetate alone or supplemented with 200 μM of calcium acetate and 100 μM of magnesium acetate (both for trace metal analysis, Sigma-Aldrich). For interaction analysis, CaM and/or caldendrin were mixed with myoVa peptide which had final concentration of 8.5 μM (low concentration) or 34 μM (high concentration). The mass spectrometer was carefully tuned for best signal quality and intensity, while keeping ion activation and unfolding minimal. Namely, electrospray voltage was kept at 1.3 kV, source desolvation temperature 250 $^\circ\text{C}$, in-source desolvation -50 V , ion transfer profile "high m/z ", analyzer profile "low m/z ", analyzer target resolution 12,500 acquiring in mass range 500–9,000 m/z . Nitrogen was used as collision gas in HCD cell at relative gas pressure setting 7.0 with gentle collisional activation by 10 V HCD voltage gradient. Raw spectra were initially averaged over at least 50 scans in Thermo Xcalibur Qual Browser 4.2.47 (Thermo Scientific) and mass deconvoluted in UniDec 4.4.1 package (Marty *et al*, 2015).

Constructs and cloning

All constructs were verified by sequencing. A complete list of expression constructs used in this study is provided in the Appendix Tables S1–S3. The TwinStrep-GFP-myosin constructs were produced by amplifying the TwinStrep-tag sequence by PCR from a TwinStrep-mCherry empty vector template (gift from A. Aher, Utrecht University), and ligating it into the pmEmerald-myoV vector using the NheI cutting site. GFP-myosin fragments for co-immunoprecipitations were amplified from the pmEmerald-myoV template by PCR. The whole myoV sequence was cut from the vector using the NotI cutting

site, and the PCR amplified fragments were re-inserted into the vector using sequence overlap and the Cold Fusion Cloning Kit (*SBI, MC010B-1*). The minimal binding region between caldendrin and myoV was narrowed down to a 49 amino-acid fragment containing the first IQ motif (aa742–791, FGKTKIFFRAGQVAYLEKLRAA CIRIQKTIRGWLLRK RYLCMQR). Underline indicates the first IQ motif sequence.

The caldendrin-tagRFP constructs were made by amplifying full length or caldendrin fragments from the pcDNA3.1/caldendrin vector and pasting them into the tagRFP-N plasmid (*Evrogen, #FP142*) using EcoRI and BamHI restriction and ligation.

pET/Calmodulin construct: Untagged human calmodulin was amplified from *Addgene* plasmid #47603 via PCR and cloned into an empty pET/T7 expression vector (gift from H.J. Kreienkamp, UKE Hamburg) using NdeI and HindIII restriction and ligation.

Immunocytochemistry

The cells were fixed in 4% Roti-Histofix (Carl Roth), 4% sucrose in PBS for 10 min at RT, and washed three times with PBS, before they were permeabilized in 0.2% Triton X-100 in PBS for 10 min. The cells were then washed 3× in PBS and blocked for 45 min at RT with blocking buffer (BB/10% horse serum, 0.1% Triton X-100 in PBS). Incubation with primary antibodies was performed in BB at 4°C overnight. After 3× washing in PBS, cells were incubated with corresponding secondary antibodies in BB for 1 h at RT. Finally, coverslips were washed 3–5× 10 min in PBS and mounted on microscope slides with Mowiol. Mowiol was prepared according to the manufacturer's protocol (9.6 g of mowiol 4–88 [Carl-Roth], 24.0 g of glycerine, 24 ml of H₂O, 48 ml of 0.2 M Tris pH 8.5, including 2.5 g of Dabco, (Sigma-Aldrich D27802).

Fixed and live cell imaging: confocal microscopy

Z-stack images of fixed and live primary hippocampal neurons were acquired either on Leica TCS SP8 and Leica TCS SP5 confocal microscopes using a 63.0× 1.40 oil objective, with the pixel size set to 85–90 nm and z-steps varied between 250 and 400 nm (fixed imaging), or on a Nikon Eclipse Ti-E spinning-disc (Yokogawa) confocal microscope (Visitron Systems GmbH) equipped with solid state lasers (405, 488, 561, and 647 nm), a 60× objective, EM-CCD cameras (Hamamatsu Photonics) and an incubation chamber for controlled environmental conditions (37°C, 5% CO₂). Live imaging of ER dynamics was performed over 10 min with a 30 sec interval between acquisitions of Z-stacks with 1 μm step size. Maximum projections of the Z-stacks were generated using Fiji/ImageJ. For the shown representative confocal images, a Gaussian filter (radius 0.5 px) was applied in ImageJ to reduce the visible background noise.

Live cell imaging: wide field and spinning disc microscopy

Wide-field and spinning-disc confocal microscopy was performed with a Nikon Eclipse Ti-E controlled by VisiView software. Samples were kept in focus with the built-in Nikon perfect focus system. The system was equipped with a 60× (Nikon, P-Apo DM 60×/1.40 oil) and a 100× TIRF objective (Nikon, ApoTIRF 100×/1.49 oil), and 488 nm, 561 nm, and 639 nm excitation lasers. Lasers were coupled to a CSU-X1 spinning disk unit via a single-mode fiber. Emission

was collected through a quad band filter (Chroma, ZET 405/488/561/647 m) followed by a motorized filter wheel (Prior Scientific) with filters for CFP (480/40 m), GFP (525/50 m), YFP (535/30 m), RFP (609/54 m), and Cy5 (700/75 m, Chroma) and captured on an Orca flash 4.0LT CMOS camera (Hamamatsu). COS7 cells were imaged with the 60× objective, neurons were imaged with the 100× objective. Time-lapse images were acquired sequentially with specified intervals.

Inducible dimerization assay in COS7 cells

COS7 cells were transfected with four plasmid constructs: KIF17(1-547)-GFP-PEX26, PEX-mRFP-FKBP, MyoVb(1-1090)-GFP-FRB, and either untagged caldendrin, or an empty control plasmid. Imaging was done 18–24 h after transfection in regular growth medium. If cells were grown on coverslips, they were placed in an attofluor cell chamber (Thermo Fisher Scientific). Correct temperature (37°C), CO₂ (5%), and humidity (90%) were maintained with a top stage incubator and an additional objective heater (Okolab). Cells with sufficient expression levels (judged by peroxisome visibility [RFP], peroxisome motility [KIF17], and the presence of myosin Vb accumulation in the cell periphery [GFP]) were selected for time-lapse live imaging. Selected cells were imaged for 20 s with a high frame rate (1 fps) before any treatment to establish baseline peroxisome motility. Then, Rapalog (A/C Heterodimerizer, *TaKaRa, #635056*) was added manually to a concentration of 100 nM to the cell medium. After a 10 min incubation, cells were imaged again for 20 s with 1 fps to determine the effect of the rapalog treatment.

Analysis of peroxisomal motility

Single particle tracking was performed with TrackMate (Tinevez et al, 2017) in Fiji (ImageJ 1.52p) with the following parameters: 300 nm particle diameter, 25- to 50-fold threshold, median filter, 1,500 nm gap, max. 2 empty, 3,000-nm jump. In MATLAB, both the cell outline and nuclear exclusion region were manually drawn. Only tracks whose average positions were within the cell outline and outside of the exclusion region were included in subsequent mean square displacement (MSD) calculations (msdalyzer, <https://github.com/tinevez/msdalyzer>). The weighted mean of all particle MSDs was calculated for each cell. Cells were only included in the final dataset if Rapalog decreased particle displacement at 20 s delay by at least 50%. Exclusion of cells was similar between control and caldendrin expressing cells. A linear fit to each weighted mean was calculated to obtain the slope.

Protein expression and purification

Calmodulin purification from *E. coli*

A single colony of *E. coli* BL21 transformed with the pET/CaM construct was used to inoculate a 5-ml of LB preculture. After overnight growth at 30°C, 2 ml of the preculture was used to inoculate a 1-l culture in LB medium and grown at 30°C for 4 h until the absorbance reached 0.5 at 600 nm. Expression of the plasmid was induced by adding 500 μM IPTG, the culture was put at 16°C and grown for about 16 h. Cells were then harvested at 5,000 g for 5 min. The pellet was resuspended in 40 ml of lysis buffer (25 mM of Tris, 5 mM of CaCl₂, 2 mM of MgCl₂, 200 μg/ml of lysozyme,

2 µg/ml of DNase) and put on a rotor for 10 min at RT. The lysate was then put on ice and sonicated for 2 × 3 min with a 7 mm sonicator at 30% with cycle set to 3 × 10%. After centrifugation at 40,000 g for 35 min, the lysate was passed over a 5 ml of HiTrap Phenyl FF (LS) column using the ÄKTA Start chromatography system. Flow rate was set to 3 ml/min and pressure to 0.03 mPa. Bound calmodulin was eluted with 25 mM of Tris, 10 mM of EDTA buffer. Binding and elution was performed 3×. In between, the column was washed with 25 mM of Tris, 5 mM of CaCl₂ buffer. The eluate was captured in 4 ml fractions, with the peak appearing in fraction 2. Fraction 2 from all 3 elution steps was pooled and dialyzed O/N at 4°C against 2 l of 25 mM of Tris, 50 mM of NaCl, 2 mM of CaCl₂ buffer. After the dialysis, the eluate was up-concentrated to 3 ml using an Amicon Ultra 3,000 MW centrifugal filter unit (Merck). Concentration assessment with a NanoDrop ($\epsilon = 2,980$, kDa = 17) resulted in an estimated concentration of 15 mg/ml.

Caldendrin purification from *E. coli*

A single colony of *E. coli* BL21 transformed with the pMXB10/Caldendrin-Intein-chitin-binding domain-tagged construct was used to inoculate a 20 ml of LB preculture. After overnight growth at 37°C, the whole preculture was used to inoculate a 1 l culture in LB medium and grown at 37°C for 2 h until the absorbance reached 0.5 at 600 nm. Expression of the plasmid was induced by adding 400 µM IPTG, the culture was put at 18°C and grown O/N for about 16 h. Cells were then harvested at 5,000 g for 5 min. The pellet was resuspended in 40 ml of intein buffer (20 mM of Tris-HCl pH 8.5, 500 mM of NaCl, 1 mM of EDTA, 0.5 mM of TCEP [tris(2-carboxyethyl)phosphine], 1× complete protease inhibitors). Then approx. 20 mg of lysozyme (100,000 U/mg) was added and after 30 min incubation on ice, the lysate was sonicated for 3 × 10 s with a 5 mm sonicator at 30% and cycle set to 80%. After the sonication, 50 U/ml of benzonase (Santa Cruz) was added, the lysate was incubated on ice for 1 h and then centrifuged at 20,000 g for 25 min. The supernatant containing the protein was incubated with 5 ml of chitin resin on a rotor at 4°C for 2 h. The protein-bound resin was then put in a column, washed with 100 ml of intein buffer and with 15 ml of elution buffer (intein buffer supplemented with 50 mM of DTT), before incubation with 7 ml of elution buffer O/N at 4°C. The eluate was collected approx. 16 h later, and dialysed for 2 h against 1 l intein buffer without TCEP, after 2 h the dialysis buffer was exchanged and left again O/N at 4°C. After dialysis, the eluate was diluted with 8 ml of 100 mM Tris pH 8, up-concentrated in a Amicon Ultra 10,000 MW centrifugal filter unit (Merck) to 2 ml, diluted with 1.1 ml of 100 mM Tris pH 8, again up-concentrated to 1.5 ml, and then ultra-centrifuged at 100,000 g for 15 min. Finally, the eluted protein was aliquoted, flash-frozen in liquid nitrogen and stored at -80°C. Yield ~ 1.5 mg from 1 l culture.

For native mass spectrometry, after the dialysis step, the protein was additionally purified by size-exclusion chromatography on a HiLoad 16/600 Superdex 75pg column (GE Healthcare) in intein buffer. To the 2 ml fraction, 4.66 ml of 100 mM Tris pH8 was added, before the samples were further concentrated to 5.8 mM in 1.5 ml using 10K cut off Amicon columns (Merck), ultracentrifuged for 15 min at 120,000 g, aliquoted, flash-frozen and stored at -80°C.

Myosin V purification from HEK293 cells

HEK293T cells were transfected with the TwinStrep-pmEmerald/Myosin V construct and harvested as described above. The cell lysate was supplemented with 2 mM EGTA and incubated on a rotor at 4°C with 40 µl of magnetic StrepTactin beads (Iba Life Sciences) for 1 h. The beads were then washed 2× with washing buffer (20 mM of Tris, 150 mM of NaCl, 0.5% Triton-X-100, 2 mM of EGTA, complete protease inhibitor cocktail [Roche]), and finally incubated with BXT elution buffer (100 mM of Tris pH8, 150 mM of NaCl, 1 mM of EDTA, 100 mM of biotin) for 10 min on ice. After the incubation period, the beads were centrifuged for 2 min at 5,000 g, and the supernatant containing the protein was used for further experiments. Yield ~ 1.5 µg protein from 10 cm HEK cell dish.

F-actin cosedimentation assay

G-actin (*Tebu bio*) was stored in G-buffer (20 mM of Tris-HCl pH 7.4, 20 µM of CaCl₂, 200 µM ATP, 1 mM of DTT) in 25 µM of aliquots at -80°C. Aliquots were slowly thawed on ice overnight the day before they were used. After thawing, actin was centrifuged at 200,000 g for 5 min at 4°C, and the supernatant was used for experiments. For polymerization, individual tubes were prepared with G-actin in a final concentration of 2 µM in G-buffer, and protein(s) of interest were added in the following concentrations: BSA 30 µM, caldendrin 0.5 µM, GFP-myosin 0.5 µM (purified from HEK293T cells as described above), in combinations as indicated in Fig 4A and B. The volume of the mixtures was adjusted to 20 µl with G-buffer. To induce polymerization, 20 µl of 2× AP-buffer (20 mM of Imidazole, 100 mM of KCl, 2 mM of MgCl₂, 8 mM of DTT, 200 µM of ATP) was added to the tubes in either 500 µM of EGTA or 50 µM of CaCl₂. The samples were then incubated for 1 h at RT to allow for polymerization. The samples were then centrifuged for 30 min at 100,000 g at 23°C. After centrifugation, 30 µl of the supernatant were removed and mixed with 4× SDS loading buffer. The remaining supernatant was discarded, and the pellet was taken up in 50 µl of 1× SDS loading buffer. The samples were then subjected to SDS-PAGE and/or western blot as described above.

In vitro F-actin gliding assay

The setup for the gliding assay was based on Preciado López *et al* (2014)'s study. Coverslips and microscope slides were cleaned using a "base piranha" solution: Milli-Q water, 30% hydrogen peroxide and 30% ammonium hydroxide were mixed in a 5:1:1 volume ratio and heated to 70°C in a glass beaker. Coverslips and microscope slides were placed in the solution using a slide-holder made of Teflon, and incubated for 10 min at 70°C. After the incubation period they were removed and rinsed 5× with Milli-Q water, and kept in 0.5 M KOH overnight or for at least 15 min, before they were dried in an oven at 70°C. Flow-channels with a width of approx. 4 mm were assembled from the dried microscope slides and coverslips using Para-film as a spacer. The flow channels were coated with PLL-PEG-biotin (SuSoS AG), and κ-casein (Sigma) in the following way: 0.1 mg/ml of PLL-PEG-biotin in PEM80 buffer (80 mM Pipes pH 6.8, 1 mM of EGTA, 4 mM of MgCl₂) was added into the flow channels and incubated for 1 h at room temperature. The channels were rinsed with 30 µl of PEM80 buffer, and 0.5 mg/ml of κ-casein

in PEM80 was added. After 7–10 min incubation, the channels were rinsed with 50 μ l of PEM80 and kept in a high humidity chamber until further use.

G-actin (*Tebu bio*) was stored in G-buffer (20 mM of Tris-HCl pH 7.4, 20 μ M of CaCl_2 , 200 μ M of ATP, 1 mM of DTT) in 25 μ M of aliquots at -80°C . Aliquots were slowly thawed on ice overnight the day before they were used. Immediately before use, they were diluted 1:1 in G-buffer, centrifuged at 120,000 g for 5 min at 4°C , and the supernatant was used for experiments. To prepare labeled F-actin, G-actin [12.5 μ M] was mixed in a ratio of approx. 3.75:1 with Alexa-561-labelled actin [10 μ M] (Thermo Fisher) by mixing 3 μ l G-actin with 1 μ l Alexa-561-labelled actin. The actin mix was centrifuged at 120,000 g for 5 min at 4°C , the supernatant was taken off and mixed with 6 μ l of G-buffer to achieve a volume of 10 μ l. To this, 10 μ l of 2x F-buffer (40 mM of Imidazole, 200 mM of KCl, 4 mM of MgCl_2 , 400 mM of DTT, 12 mg/ml of glucose (w/v), 80 μ g/ml of catalase, 400 μ g/ml of glucose oxidase, 1.6 mM of ATP) was added to achieve a “1 \times ” concentration of the F-buffer. Actin was left to polymerize for 20 min at room temperature in a dark chamber before use.

For the myosin V gliding assay, 2 μ l of F-actin (as described above) were taken up in 13 μ l of 1 \times F-buffer (20 mM of Imidazole, 100 mM of KCl, 2 mM of MgCl_2 , 200 mM of DTT, 6 mg/ml of glucose (w/v), 40 μ g/ml of catalase, 200 μ g/ml of glucose oxidase, 0.8 mM of ATP) and flown into the flow channel. The filaments were left to settle for 5 min, then 2 μ l of freshly purified GFP-myosin V (as above) were taken up in 20 μ l of 1 \times F-buffer and flown into the channel. The channel was left to settle for 5 min, before gliding of actin filaments was imaged. Time-lapse imaging was performed on a spinning-disc confocal with a Nikon Eclipse Ti-E as described under “Live cell imaging,” with 1 frame per second for 2–3 min. Other components were added to the channel together with myosin in the following final concentrations [stock]: Calmodulin 30 μ M, Calendrin 5 μ M (in G-Buffer), CaCl_2 200 μ M, Mg-ATP 2.5 mM.

With all components added, the final buffer composition was 16.75 mM of Tris pH 7.8, 20 mM of Imidazole, 15 mM of NaCl, 100 mM of KCl, 100 μ M of EDTA, 3.18 mM of Mg-ATP, 2 mM of MgCl_2 , 207 μ M of CaCl_2 , 200 mM of DTT, 6 mg/ml of glucose, 40 μ g/ml of catalase, 200 μ g/ml of glucose oxidase. Due to its high affinity to calcium (Henzl *et al*, 2003; O'Brien *et al*, 2015), we estimate that the 100 μ M of EDTA chelated roughly 100 μ M Ca^{2+} , leaving around 107 μ M free calcium. According to the UC Davis Maxchelator online calculator “Ca-Mg-ATP-EGTA Calculator,” under those conditions, roughly 45% of the 107 μ M of calcium will be chelated by ATP, which leaves around 59 μ M of free calcium in the buffer.

<https://somapp.ucdmc.ucdavis.edu/pharmacology/bers/maxchelator/CaMgATPEGTA-NIST-Plot.htm>

Analysis of F-actin gliding

In order to assess the percentage of actin filaments that was being actively transported (“gliding”) as opposed to being immobile, the first and 30th frame of a time lapse stack were overlaid in different colors (first frame = red, 30th frame = green). Filaments that had moved, detached, or landed during this time span appear either red or green, whereas immobile filaments appear yellow. Those filaments were counted manually, and the percentage of total filaments was calculated.

To compare the gliding velocity in the presence or absence of calendrin, we used the “manual tracking” plug-in of Fiji/ImageJ (Cordelières, 2005) to track individual actin filaments by one of their ends. Frame-to-frame velocity was calculated from these tracks.

Statistical analysis

Statistical analysis was performed in Prism 6.05 (GraphPad; all other tests). Detailed specifications about the type of test, significance levels, n numbers, and biological replicates are provided in the figure legends. Experimental repeats and n numbers per experiment were chosen according to experience with effect size. Data are represented as mean \pm SEM throughout the manuscript. The data were tested for normality using the D’Agostino-Pearson test (Prism) and accordingly subjected to parametric (t -test, ANOVA) or non-parametric tests (Mann–Whitney test, Kruskal–Wallis test) for significance. The analysis of the calendrin knock-out mice data was done blindly.

Data availability

Protein interaction AP-MS data are provided in Dataset EV1. The mass spectrometry proteomics data have been deposited to the ProteomeXchange Consortium via the PRIDE partner repository with the dataset identifier PXD029427 (<http://www.ebi.ac.uk/pride/archive/projects/PXD029427>). The native mass spectrometry data have been deposited on Zenodo under <https://doi.org/10.5281/zenodo.5652931>.

Expanded View for this article is available online.

Acknowledgements

The authors thank W. Wagner (*GFP-myo Va fl*), T.G. Oertner (*ER-tDimer2*), and L. Kapitein and C. Hoogenraad (*KIF17₁₋₅₄₇-GFP-PEX26*, *PEX-mRFP-FKBP*, *MyoVb₁₋₁₀₉₀-GFP-FRB*) for sharing plasmids. jGCAMP7s was a gift from D. Kim (*Addgene #104463*). They further thank S. Hochmuth for preparing mouse neuronal cultures, J. Bär and M. Andres-Alonso for preparing rat neuronal cultures, R. Raman for providing the purified calendrin Ca^{2+} -binding mutant protein, the UKE Microscopy Imaging Facility (UMIF) and the Leibniz-Institut für Neurobiologie Magdeburg (LIN) for access and use of their spinning disc and confocal microscopes, Prof. A. Itzen for help with purification of the calendrin protein, and Dr. I. Hermans-Borgmeyer for help with the calendrin knockout mouse line. This work was supported by the Deutsche Forschungsgemeinschaft (DFG Emmy Noether Programme MI1923/1-2, FOR2419 TP2, SFB877 B12 and Excellence Strategy – EXC-2049–390688087) and Hertie Network of Excellence in Clinical Neuroscience and Excellence Strategy Program. The Leibniz Institute for Experimental Virology (HPI) is supported by the Freie und Hansestadt Hamburg and the Bundesministerium für Gesundheit (BMG). AKa gratefully acknowledges a postdoctoral fellowship from the Alexander von Humboldt Foundation. CU acknowledges funding through EU Horizon 2020 ERC StG-2017 759661 SPOCK’S MS. Open Access funding enabled and organized by Projekt DEAL.

Author contributions

AKo performed biochemical and cell biological experiments; AKo and NH cloned expression constructs and performed co-immunoprecipitations; AKa and CU performed and analyzed native mass spectrometry; MB performed and

analyzed CD spectroscopy; DHWD and JAAD performed mass spectrometric analysis of the caldendrin interactome; JG performed mass spectrometric, ER-tracking and MSD analysis; YH prepared primary mouse neurons. AKo, JG and MM analyzed the results, prepared figures and wrote the manuscript. CU, KG and MM acquired funding and MM coordinated the project.

Conflict of interest

The authors declare that they have no conflict of interest.

References

- van Bommel B, Konietzny A, Kobler O, Bär J, Mikhaylova M (2019) F-actin patches associated with glutamatergic synapses control positioning of dendritic lysosomes. *EMBO J* 38: 1–17
- Bowen AB, Bourke AM, Hiester BG, Hanus C, Kennedy MJ (2017) Golgi-independent secretory trafficking through recycling endosomes in neuronal dendrites and spines. *Elife* 6: 1–27
- Bowler BE (2012) Residual structure in unfolded proteins. *Curr Opin Struct Biol* 22: 4–13
- Cao QJ, Zhang N, Zhou R, Yao LL, Li XD (2019) The cargo adaptor proteins RILPL2 and melanophilin co-regulate myosin-5a motor activity. *J Biol Chem* 294: 11333–11341
- Chazin WJ (2011) Relating form and function of EF-hand calcium binding proteins. *Acc Chem Res* 44: 171–179
- Chirillo MA, Waters MS, Lindsey LF, Bourne JN, Harris KM (2019) Local resources of polyribosomes and SER promote synapse enlargement and spine clustering after long-term potentiation in adult rat hippocampus. *Sci Rep* 9: 1–14
- Cordelières F (2005) *Manual tracking, a plug-in for ImageJ software*. Orsay: Institut Curie
- Coureau PD, Sweeney HL, Houdusse A (2004) Three myosin V structures delineate essential features of chemo-mechanical transduction. *EMBO J* 23: 4527–4537
- Dana H, Sun Y, Mohar B, Hulse BK, Kerlin AM, Hasseman JP, Tsegaye G, Tsang A, Wong A, Patel R et al (2019) High-performance calcium sensors for imaging activity in neuronal populations and microcompartments. *Nat Methods* 16: 649–657
- Deller T, Korte M, Chabanis S, Drakew A, Schwegler H, Stefani GG, Zuniga A, Schwarz K, Bonhoeffer T, Zeller R et al (2003) Synaptopodin-deficient mice lack a spine apparatus and show deficits in synaptic plasticity. *Proc Natl Acad Sci USA* 100: 10494–10499
- Dieterich DC, Karpova A, Mikhaylova M, Zdobnova I, König I, Landwehr M, Kreutz M, Smalla K-H, Richter K, Landgraf P et al (2008) Caldendrin-Jacob: a protein liaison that couples NMDA receptor signalling to the nucleus. *PLoS Biol* 6: 0286–0306
- Esteves da Silva M, Adrian M, Schätzle P, Lipka J, Watanabe T, Cho S, Futai K, Wierenga CJ, Kapitein LC, Hoogenraad CC (2015) Positioning of AMPA receptor-containing endosomes regulates synapse architecture. *Cell Rep* 13: 933–943
- Faas GC, Raghavachari S, Lisman JE, Mody I (2011) Calmodulin as a direct detector of Ca²⁺ signals. *Nat Neurosci* 14: 301–304
- Flick TG, Cassou CA, Chang TM, Williams ER (2012) Solution additives that desalt protein ions in native mass spectrometry. *Anal Chem* 84: 7511–7517
- Goo MS, Sancho L, Slepak N, Boassa D, Deerinck TJ, Ellisman MH, Bloodgood BL, Patrick GN (2017) Activity-dependent trafficking of lysosomes in dendrites and dendritic spines. *J Cell Biol* : 1–15
- Greenfield NJ (2007) Using circular dichroism spectra to estimate protein secondary structure. *Nat Protoc* 1: 2876–2890
- Hammer JA, Wagner W (2013) Functions of class v myosins in neurons. *J Biol Chem* 288: 28428–28434
- Hanus C, Kochen L, Tom Dieck S, Racine V, Sibarita JB, Schuman EM, Ehlers MD (2014) Synaptic control of secretory trafficking in dendrites. *Cell Rep* 7: 1771–1778
- Hedges JB, Vahidi S, Yue X, Konermann L (2013) Effects of ammonium bicarbonate on the electrospray mass spectra of proteins: evidence for bubble-induced unfolding. *Anal Chem* 85: 6469–6476
- Heissler SM, Sellers JR (2015) Myosin light chains: teaching old dogs new tricks. *Bioarchitecture* 4: 169–188
- Heissler SM, Sellers JR (2016) Various themes of myosin regulation. *J Mol Biol* 428: 1927–1946
- Henzl MT, Larson JD, Agah S (2003) Estimation of parvalbumin Ca²⁺- and Mg²⁺-binding constants by global least-squares analysis of isothermal titration calorimetry data. *Anal Biochem* 319: 216–233
- Holbro N, Grunditz A, Oertner TG (2009) Differential distribution of endoplasmic reticulum controls metabotropic signaling and plasticity at hippocampal synapses. *Proc Natl Acad Sci USA* 106: 15055–15060
- Homma K, Saito J, Ikebe R, Ikebe M (2000) Ca²⁺-dependent regulation of the motor activity of myosin V. *J Biol Chem* 275: 34766–34771
- Iavarone AT, Udekwu OA, Williams ER (2004) Buffer loading for counteracting metal salt-induced signal suppression in electrospray ionization. *Anal Chem* 76: 3944–3950
- Kapitein LC, van Bergeijk P, Lipka J, Keijzer N, Wulf PS, Katrukha EA, Akhmanova A, Hoogenraad CC (2013) Myosin-V opposes microtubule-based cargo transport and drives directional motility on cortical actin. *Curr Biol* 23: 828–834
- Kapitein LC, Yau KW, Hoogenraad CC (2010) Microtubule dynamics in dendritic spines. *Methods Cell Biol* 97: 111–132
- Kelly SM, Jess TJ, Price NC (2005) How to study proteins by circular dichroism. *Biochim Biophys Acta Proteins Proteomics* 1751: 119–139
- Kennedy MJ, Hanus C (2019) Architecture and dynamics of the neuronal secretory network. *Annu Rev Cell Dev Biol* 35: 543–566
- Kim KY, Scholl ES, Liu X, Shepherd A, Haeseleer F, Lee A (2014) Localization and expression of CaBP1/caldendrin in the mouse brain. *Neuroscience* 268: 33–47
- Kneussel M, Wagner W (2013) Myosin motors at neuronal synapses: drivers of membrane transport and actin dynamics. *Nat Rev Neurosci* 14: 233–247
- Koide H, Kinoshita T, Tanaka Y, Tanaka S, Nagura N, Meyer Zu Hörste G, Miyagi A, Ando T (2006) Identification of the single specific IQ motif of myosin V from which calmodulin dissociates in the presence of Ca²⁺. *Biochemistry* 45: 11598–11604
- Konietzny A, González-Gallego J, Bär J, Perez-Alvarez A, Drakew A, Demmers JAA, Dekkers DHW, Hammer JA, Frotscher M, Oertner TG et al (2019) Myosin V regulates synaptopodin clustering and localization in the dendrites of hippocampal neurons. *J Cell Sci* 132: 1–16
- Krementsov DN, Krementsova EB, Trybus KM (2004) Myosin V: regulation by calcium, calmodulin, and the tail domain. *J Cell Biol* 164: 877–886
- Krichel B, Bylapudi G, Schmidt C, Blanchet C, Schubert R, Brings L, Koehler M, Zenobi R, Svergun D, Lorenzen K et al (2021) Hallmarks of alpha- and betacoronavirus non-structural protein 7+8 complexes. *Sci Adv* 7: eabf1004
- Laube G, Seidenbecher CI, Richter K, Dieterich DC, Hoffmann B, Landwehr M, Smalla KH, Winter C, Böckers TM, Wolf G et al (2002) The neuron-specific Ca²⁺-binding protein caldendrin: gene structure, splice isoforms, and

- expression in the rat central nervous system. *Mol Cell Neurosci* 19: 459–475
- Li XD, Ikebe R, Ikebe M (2005) Activation of myosin Va function by melanophilin, a specific docking partner of myosin Va. *J Biol Chem* 280: 17815–17822
- Li W, Qin M, Tie Z, Wang W (2011) Effects of solvents on the intrinsic propensity of peptide backbone conformations. *Phys Rev E Stat Nonlin Soft Matter Phys* 84: 1–9
- Li C, Enomoto M, Rossi AM, Seo MD, Rahman T, Stathopoulos PB, Taylor CW, Ikura M, Ames JB (2013) CaBP1, a neuronal Ca²⁺ sensor protein, inhibits inositol trisphosphate receptors by clamping intersubunit interactions. *Proc Natl Acad Sci USA* 110: 8507–8512
- Lu Z, Shen M, Cao Y, Zhang HM, Yao LL, Li XD (2012) Calmodulin bound to the first IQ motif is responsible for calcium-dependent regulation of myosin 5a. *J Biol Chem* 287: 16530–16540
- Marty MT, Baldwin AJ, Marklund EG, Hochberg GKA, Benesch JLP, Robinson CV (2015) Bayesian deconvolution of mass and ion mobility spectra: from binary interactions to polydisperse ensembles. *Anal Chem* 87: 4370–4376
- Maschi D, Gramlich MW, Klyachko VA (2018) Myosin V functions as a vesicle tether at the plasma membrane to control neurotransmitter release in central synapses. *Elife* 7: 1–30
- Micsonai A, Wien F, Bulyáki É, Kun J, Moussong É, Lee YH, Goto Y, Réfrégiers M, Kardos J (2018) BeStSel: a web server for accurate protein secondary structure prediction and fold recognition from the circular dichroism spectra. *Nucleic Acids Res* 46: W315–W322
- Mikhaylova M, Sharma Y, Reissner C, Nagel F, Aravind P, Rajini B, Smalla KH, Gundelfinger ED, Kreutz MR (2006) Neuronal Ca²⁺ signaling via caldendrin and calneurons. *Biochim Biophys Acta Mol Cell Res* 1763: 1229–1237
- Mikhaylova M, Bera S, Kobler O, Frischknecht R, Kreutz MR (2016) A dendritic golgi satellite between ERGIC and retromer. *Cell Rep* 14: 189–199
- Mikhaylova M, Bär J, van Bommel B, Schätzle P, YuanXiang PingAn, Raman R, Hradsky J, Konietzny A, Loktionov EY, Reddy PP et al (2018) Caldendrin directly couples postsynaptic calcium signals to actin remodeling in dendritic spines. *Neuron* 97: 1110–1125
- Mollica L, Bessa LM, Hanouille X, Jensen MR, Blackledge M, Schneider R (2016) Binding mechanisms of intrinsically disordered proteins: theory, simulation, and experiment. *Front Mol Biosci* 3: 1–18
- Mundel P, Heid HW, Mundel TM, Krüger M, Reiser J, Kriz W (1997) Synaptopodin: an actin-associated protein in telencephalic dendrites and renal podocytes. *J Cell Biol* 139: 193–204
- Mundhenk J, Fusi C, Kreutz MR (2019) Caldendrin and calneurons—EF-hand CaM-like calcium sensors with unique features and specialized neuronal functions. *Front Mol Neurosci* 2: 1–9
- Nakamura T, Barbara JG, Nakamura K, Ross WN (1999) Synergistic release of Ca²⁺ from IP₃-sensitive stores evoked by synaptic activation of mGluRs paired with backpropagating action potentials. *Neuron* 24: 727–737
- Nascimento AAC, Cheney RE, Tauhata SBF, Larson RE, Mooseker MS (1996) Enzymatic characterization and functional domain mapping of brain myosin-V. *J Biol Chem* 271: 17561–17569
- Nguyen HA, Higuchi H (2005) Motility of myosin V regulated by the dissociation of single calmodulin. *Nat Struct Mol Biol* 12: 127–132
- O'Brien LC, Root HB, Wei CC, Jensen D, Shabestary N, De Meo C, Eder DJ (2015) M²⁺•EDTA binding affinities: a modern experiment in thermodynamics for the physical chemistry laboratory. *J Chem Educ* 92: 1547–1551
- Padamsey Z, McGuinness L, Bardo SJ, Reinhart M, Tong R, Hedegaard A, Hart ML, Emptage NJ (2017) Activity-dependent exocytosis of lysosomes regulates the structural plasticity of dendritic spines. *Neuron* 93: 132–146
- Perez-Alvarez A, Yin S, Schulze C, Hammer JA, Wagner W, Oertner TG (2020) Endoplasmic reticulum visits highly active spines and prevents runaway potentiation of synapses. *Nat Commun* 11: 1–10
- Preciado López M, Huber F, Grigoriev I, Steinmetz MO, Akhmanova A, Dogterom M, Koenderink GH (2014) *In vitro* reconstitution of dynamic microtubules interacting with actin filament networks. *Methods Enzymol* 540: 301–320
- Raghuram V, Sharma Y, Kreutz MR (2012) Ca²⁺ sensor proteins in dendritic spines: a race for Ca²⁺. *Front Mol Neurosci* 5: 1–12
- Reddy PP, Raghuram V, Hradsky J, Spilker C, Chakraborty A, Sharma Y, Mikhaylova M, Kreutz MR (2014) Molecular dynamics of the neuronal EF-Hand Ca²⁺-sensor caldendrin. *PLoS One* 9: e103186
- Segal M, Korkotian E (2014) Endoplasmic reticulum calcium stores in dendritic spines. *Front Neuroanat* 8: 1–7
- Seidenbecher CI, Langnaese K, Sanmartí-Vila L, Boeckers TM, Smalla KH, Sabel BA, Garner CC, Gundelfinger ED, Kreutz MR (1998) Caldendrin, a novel neuronal calcium-binding protein confined to the somato-dendritic compartment. *J Biol Chem* 273: 21324–21331
- Sellers JR, Thirumurugan K, Sakamoto T, Hammer JA, Knight PJ (2008) Calcium and cargoes as regulators of myosin 5a activity. *Biochem Biophys Res Commun* 369: 176–181
- Shen M, Zhang N, Zheng S, Zhang WB, Zhang HM, Lu Z, Su QP, Sun Y, Ye K, Li X-D (2016) Calmodulin in complex with the first IQ motif of myosin-5a functions as an intact calcium sensor. *Proc Natl Acad Sci USA* 113: E5812–E5820
- Smalla KH, Seidenbecher CI, Tischmeyer W, Schicknick H, Wyneken U, Böckers TM, Gundelfinger ED, Kreutz MR (2003) Kainate-induced epileptic seizures induce a recruitment of caldendrin to the postsynaptic density in rat brain. *Mol Brain Res* 116: 159–162
- Tinevez JY, Perry N, Schindelin J, Hoopes GM, Reynolds GD, Laplantine E, Bednarek SY, Shorte SL, Eliceiri KW (2017) TrackMate: an open and extensible platform for single-particle tracking. *Methods* 115: 80–90
- Tippens AL, Lee A (2007) Caldendrin, a neuron-specific modulator of Cav1.2 (L-type) Ca²⁺ channels. *J Biol Chem* 282: 8464–8473
- Trybus KM, Gushchin MI, Lui H, Hazelwood L, Kremetsova EB, Volkmann N, Hanein D (2007) Effect of calcium on calmodulin bound to the IQ motifs of myosin V. *J Biol Chem* 282: 23316–23325
- Trybus KM (2008) Myosin V from head to tail. *Cell* 65: 1378–1389
- Wagner W, Brenowitz SD, Hammer JAI (2011) Myosin-Va transports the endoplasmic reticulum into the dendritic spines of purkinje neurons. *Nat Cell Biol* 1: 40–48
- Wang Z, Edwards JG, Riley N, Provance DW, Karcher R, Li X-D, Davison IG, Ikebe M, Mercer JA, Kauer JA et al (2008) Myosin Vb mobilizes recycling endosomes and AMPA receptors for postsynaptic plasticity. *Cell* 135: 535–548
- Wiegert JS, Pulin M, Gee CE, Oertner TG (2018) The fate of hippocampal synapses depends on the sequence of plasticity-inducing events. *Elife* 7: 1–18
- Wilm M, Shevchenko A, Houthaev T, Breit S, Schweigerer L, Fotsis T, Mann M (1996) Femtomole sequencing of proteins from polyacrylamide gels by nano-electrospray mass spectrometry. *Nature* 379: 466–469
- Wingard JN, Chan J, Bosanac I, Haeseleer F, Palczewski K, Ikura M, Ames JB (2005) Structural analysis of Mg²⁺ and Ca²⁺ binding to CaBP1,

- a neuron-specific regulator of calcium channels. *J Biol Chem* 280: 37461–37470
- Yoshii A, Zhao JP, Pandian S, van Zundert B, Constantine-Paton M (2013) A myosin Va mutant mouse with disruptions in glutamate synaptic development and mature plasticity in visual cortex. *J Neurosci* 33: 8472–8482
- Yoshimura A, Fujii R, Watanabe Y, Okabe S, Fukui K, Takumi T (2006) Myosin-Va facilitates the accumulation of mRNA/protein complex in dendritic spines. *Curr Biol* 16: 2345–2351
- Yu MC, Shin HK, Chung S, Dae YU, Myoung KP (2006) Regional interaction of endoplasmic reticulum Ca^{2+} signals between soma and dendrites through rapid luminal Ca^{2+} diffusion. *J Neurosci* 26: 12127–12136
- Zhang M, Abrams C, Wang L, Gizzi A, He L, Lin R, Chen Y, Loll PJ, Pascal JM, Zhang JF (2012) Structural basis for calmodulin as a dynamic calcium sensor. *Structure* 20: 911–923
- Zhong L, Johnson WC (1992) Environment affects amino acid preference for secondary structure. *Proc Natl Acad Sci USA* 89: 4462–4465



License: This is an open access article under the terms of the Creative Commons Attribution-NonCommercial-NoDerivs License, which permits use and distribution in any medium, provided the original work is properly cited, the use is non-commercial and no modifications or adaptations are made.